

Bachelor Thesis



**Czech
Technical
University
in Prague**

F3

**Faculty of Electrical Engineering
Department of Electromagnetic Field**

Collinear Slot Antennas with High Directivity

David Buchtel

**Supervisor: Doc. Ing. Pavel Hazdra, Ph.D.
May 2024**

I. OSOBNÍ A STUDIJNÍ ÚDAJE

Příjmení: **Buchtel** Jméno: **David** Osobní číslo: **507260**
Fakulta/ústav: **Fakulta elektrotechnická**
Zadávající katedra/ústav: **Katedra elektromagnetického pole**
Studijní program: **Elektronika a komunikace**

II. ÚDAJE K BAKALÁŘSKÉ PRÁCI

Název bakalářské práce:

Štěrbinové kolineární antény s vysokou směrovostí

Název bakalářské práce anglicky:

Collinear Slot Antennas with High Directivity

Pokyny pro vypracování:

Prostudujte literaturu v oblasti kolineárních antén, zaměřte se na tzv. Franklinovu řadu realizovanou pomocí štěrbin. Nasimulujte a porovnejte vlastnosti několika vybraných struktur včetně vhodného reflektoru/dutiny. Optimalizujte zisk struktury nejprve pomocí jednoduchého analytického modelu a posléze v simulátoru elmag. pole. Navrženou anténu vyrobte a vlastnosti ověřte měřeními.

Seznam doporučené literatury:

- [1] <https://ieeexplore.ieee.org/document/8386759>
- [2] <https://ieeexplore.ieee.org/document/4232614>
- [3] <https://ieeexplore.ieee.org/document/1506807>
- [4] <https://ieeexplore.ieee.org/document/9703717>

Jméno a pracoviště vedoucí(ho) bakalářské práce:

doc. Ing. Pavel Hazdra, Ph.D. FEL ČVUT v Praze, K 13117

Jméno a pracoviště druhé(ho) vedoucí(ho) nebo konzultanta(ky) bakalářské práce:

Datum zadání bakalářské práce: **06.02.2024**

Termín odevzdání bakalářské práce: **24.05.2024**

Platnost zadání bakalářské práce: **21.09.2025**

doc. Ing. Pavel Hazdra, Ph.D.
podpis vedoucí(ho) práce

podpis vedoucí(ho) ústavu/katedry

prof. Mgr. Petr Páta, Ph.D.
podpis děkana(ky)

III. PŘEVZETÍ ZADÁNÍ

Student bere na vědomí, že je povinen vypracovat bakalářskou práci samostatně, bez cizí pomoci, s výjimkou poskytnutých konzultací. Seznam použité literatury, jiných pramenů a jmen konzultantů je třeba uvést v bakalářské práci.

Datum převzetí zadání

Podpis studenta

Acknowledgements

I want to thank my thesis supervisor, Ing. Pavel Hazdra, Ph.D., for his helpful guidance, invaluable suggestions, and countless consults, which immensely helped me to write this thesis.

I also want to thank all the teachers from the Antennas Design and Technology (B2M17NKA) course, which has elevated my knowledge of antennas beyond the basics taught at the bachelor level.

Then I also want to thank Ing. Václav Kabourek, Ph.D., for helping me with the antenna measurements within the department's anechoic chamber, as well as my friend Matěj Vajnar for 3D-printing all the antenna holders and other plastic pieces.

Lastly, I want to thank my family for all the support I have received from them during my studies.

Declaration

I declare that the presented work was developed independently and that I have listed all sources of information used within it in accordance with the methodical instructions for observing the ethical principles in the preparation of university theses.

David Buchtel,
Prague, May 22. 2024

Abstract

This thesis looks into a slot antenna with a slot shaped like a Franklin antenna. Such an antenna combines the directional benefits of a simple slot antenna and a Franklin antenna. This antenna can be implemented as a printed circuit board (PCB) antenna, and unlike in the previous works, it is shown that a cutout in the PCB substrate itself can benefit the antenna performance. These Franklin slot antennae can be easily matched to an impedance of 50Ω without any balun necessary and attain an operating bandwidth of 20 %.

Two reflectors for use with these antennas are also examined as they make the Franklin slot antennas radiate unidirectionally and increase their directivity.

Keywords: Franklin antenna, collinear antenna, slot antenna, CST Studio Suite, PCB antenna, high directivity antenna, reflector antenna

Supervisor: Doc. Ing. Pavel Hazdra, Ph.D.
FEE CTU in Prague, K13137

Abstrakt

Tato práce se zabývá štěrbinovými anténami se štěrbinou tvaru Franklinovy antény. Taková anténa kombinuje výhody prosté štěrbinové antény a Franklinovy antény z pohledu směrovosti. Tato anténa se dá implementovat jako anténa na desce plošných spojů, a na rozdíl od předchozích prací bylo ukázáno, že pokud je štěrbina i v substrátu desky plošných spojů, tak se anténa chová lépe. Tyto Franklinovy štěrbinové antény lze jednoduše přizpůsobit na impedanci 50Ω bez potřeby použití balunu. Takovéto antény dosahují pracovní šířky pásma kolem 20 %.

Dále byly prozkoumány ještě dva reflektory pro použití s těmito anténami, díky kterým pak Franklinova štěrbinová anténa vyzařuje jednosměrově a s větší směrovostí.

Klíčová slova: Franklinova anténa, kolineární anténa, štěrbinová anténa, CST Studio Suite, PCB anténa, anténa s vysokou směrovostí, anténa s reflektorem

Překlad názvu: Štěrbínové kolineární antény s vysokou směrovostí

Contents

Introduction	1
1 Fundamental antenna characteristics	3
1.1 Input characteristics	3
1.2 Radiation characteristics	4
2 Commonly used antenna structures	7
2.1 Electric dipole	7
2.2 Slot antenna	9
2.3 Antenna array	11
2.4 Franklin antenna	13
3 Theoretical models for slot antennas	15
3.1 Slot antenna as an aperture	15
3.2 Effects of finite ground plane . . .	20
3.3 Slot antenna with a reflector . . .	22
3.4 Approximate model for the Franklin slot antenna	23
4 Franklin slot antenna as a thin PEC sheet	25
4.1 Three-element Franklin slot antenna	25
4.2 Five-element Franklin slot antenna	27
4.3 Franklin slot antennas with more elements	30
5 Franklin slot antenna on FR4 substrate	31
5.1 Effects of FR4 substrate	31
5.2 Model with coaxial feed	34
5.3 Models for realised antennas . . .	35
5.4 Reflectors for Franklin slot antennas	39
6 Antenna realisation and measurements	43
6.1 Realisation of antennas	43
6.2 Measurement setup	45
6.3 Measurements of realised antennas	46
Conclusion	51
Bibliography	53

Figures

<p>1.1 Antenna operating region with S_{11} lower than -10 dB 4</p> <p>1.2 Spherical coordinates used in this thesis 4</p> <p>1.3 Radiation pattern with highlighted parameters 5</p> <p>1.4 Antenna operating region with less than 3 dB decrease of directivity 6</p> <p>2.1 Dipole antenna 7</p> <p>2.2 Radiation pattern in E plane for different dipole lengths 8</p> <p>2.3 Dipole input resistance and reactance for different values of w 8</p> <p>2.4 Slot antenna 9</p> <p>2.5 Slot antenna input characteristics for different values of w_{slot} 10</p> <p>2.6 Antenna array formed by two dipoles 11</p> <p>2.7 Radiation characteristics of two half-wavelength dipoles 12</p> <p>2.8 Three-element Franklin antenna 13</p> <p>2.9 Radiation characteristics of Franklin antennas with N elements 14</p> <p>2.10 Three-element Franklin antenna input impedance for different values of w 14</p> <p>3.1 Aperture on an infinite ground plane with uniform E-field distribution 16</p> <p>3.2 Radiation pattern for slot antenna with uniform E-field distribution 17</p> <p>3.3 Aperture on an infinite ground plane with cosine E-field distribution 18</p> <p>3.4 Radiation pattern for slot antenna with cosine E-field distribution 19</p> <p>3.5 Comparison between analytical and simulated models of slot antennas 20</p> <p>3.6 Uniform empirical H-pattern model for both planes 21</p> <p>3.7 Uniform empirical model with correction 21</p> <p>3.8 Simple model with a flat reflector 22</p> <p>3.9 Uniform empirical model with a flat reflector and correction 22</p>	<p>3.10 Simple model for a five-element Franklin slot antenna 24</p> <p>3.11 Model for a five-element Franklin slot antenna with corrections 24</p> <p>4.1 Three-element Franklin slot antenna 25</p> <p>4.2 Three-element Franklin slot performance for different w_{slot} 25</p> <p>4.3 Three-element Franklin slot performance for different w_{gnd} 26</p> <p>4.4 Three-element Franklin slot performance for different w_{gap} 26</p> <p>4.5 Three-element Franklin slot performance for different l_{gnd} 26</p> <p>4.6 Parameters of simulated three-element Franklin slot antenna 27</p> <p>4.7 Variants of five-element Franklin slot antennas 27</p> <p>4.8 Performance of the three phasing element configurations 28</p> <p>4.9 Radiation pattern for Option A five-element Franklin slot antenna 28</p> <p>4.10 Five-element antenna with phasing elements facing one direction 29</p> <p>4.11 Performance of antenna with phasing elements in one direction 29</p> <p>4.12 Parameters of antennas with N radiating elements 30</p> <p>5.1 Comparison between PEC and FR4 Franklin slot antenna models 31</p> <p>5.2 Performance of antennas with additional metalisation 32</p> <p>5.3 Franklin slot antenna performance for different substrate ϵ_r 33</p> <p>5.4 Franklin slot antenna performance for different h_{FR4} 33</p> <p>5.5 Franklin slot antenna performance for different h_{Cu} 33</p> <p>5.6 Coaxial feed modelled for the antenna 34</p> <p>5.7 Franklin slot antenna S parameters for different coaxial r_a 34</p> <p>5.8 Realised 2.5 GHz Franklin slot antenna 35</p>
--	--

5.9 Performance of the realised 2.5 GHz Franklin slot antenna	35	6.9 S_{11} for the 10 GHz antenna with one-sided phasing elements	46
5.10 Realised 10 GHz Franklin slot antenna	36	6.10 S_{11} for the 10 GHz first iteration antenna with the flat reflector	47
5.11 Performance of the realised 10 GHz Franklin slot antenna	36	6.11 S_{11} for the 10 GHz second iteration antenna with the V reflector	47
5.12 Realised 10 GHz antenna with phasing elements in one direction .	37	6.12 Broadband performance of the 10 GHz second iteration antenna	47
5.13 Performance of the realised 10 GHz antenna with phasing elements in one direction	37	6.13 Gain for the 2.5 GHz antenna .	48
5.14 Realised first iteration of the 10 GHz antenna	38	6.14 Gain for the 10 GHz second iteration antenna	48
5.15 Performance of the realised 10 GHz first iteration antenna	38	6.15 Gain for the 10 GHz antenna with one-sided phasing elements	48
5.16 10 GHz Franklin slot antenna with a flat reflector	39	6.16 Gain for the 10 GHz first iteration antenna with the flat reflector	49
5.17 Flat reflector antenna performance for different w_{ref}	39	6.17 Gain for the 10 GHz second iteration antenna with the V reflector	49
5.18 Flat reflector antenna performance for different d_{ref}	40	6.18 Radiation patterns for the following antennas	49
5.19 Performance of 10 GHz antennas with the flat reflector	40	6.19 Radiation patterns for the 10 GHz second iteration antenna	50
5.20 10 GHz Franklin slot antenna with a V-shaped reflector	41	6.20 Radiation patterns for 10 GHz antenna with the V-shaped reflector	50
5.21 V-shaped reflector antenna performance for different θ_{ref}	41		
5.22 Franklin slot antenna performance for different w_{ref}	42		
5.23 Performance of 10 GHz antennas with the V-shaped reflector	42		
6.1 10 GHz Franklin slot antenna PCB designed in KiCad software	43		
6.2 All four realised versions of 10 GHz Franklin slot antennas	43		
6.3 2.5 GHz Franklin slot antenna with its holder	44		
6.4 Flat reflector and the V-shaped reflector for 10 GHz antennas	44		
6.5 Setup used for measuring radiation patterns and directivity	45		
6.6 Antenna with a flat reflector in the RF anechoic chamber	45		
6.7 S_{11} for the 2.5 GHz antenna . . .	46		
6.8 S_{11} for the 10 GHz second iteration antenna	46		

Tables

2.1 Properties of electric and magnetic dipoles as linked through duality	9
2.2 Approximate directivity of a Franklin antenna with N elements	13



Introduction


The half-wave dipole antenna is an omnidirectional antenna with a directivity of 2.15 dBi. If we need an antenna for longer ranges, we should use a different one with a higher directivity to reduce the free space loss. We could instead use a slot antenna with a rectangular slot cutout. A well-designed slot antenna can achieve a directivity of around 6 dBi and a higher bandwidth than the half-wave dipole [1]. Alternatively, we could use a Franklin antenna named after C. S. Franklin instead [2]. Franklin antenna comprises half-wave radiating elements and U-shaped phasing elements of quarter-wave height. The radiating elements thus form a collinear array, leading to increased directivity, while the phasing elements cancel out the opposite phase of the current distribution. The directivity of a Franklin antenna depends on the number of radiating elements, but a five-element Franklin antenna has a directivity of 7 dBi.

This thesis aims to combine the principles of a slot antenna and a Franklin antenna into a single Franklin slot antenna to create an antenna with an even higher directivity. Such an antenna can be realised as a conductive sheet or a PCB (printed circuit board) antenna. The Franklin slot antennas were examined in [3] and [4]. In [5], a variation of the Franklin slot antenna with a circular polarisation was also examined. However, all the previous works have fed the Franklin slot antennas with coplanar waveguides, whilst in this thesis, a coaxial cable feed was used, similarly as for the slot antenna in [1]. Also, these Franklin slot antennas from the previous works were realised on a solid FR4 substrate, whilst antennas in this thesis have a cutout in the substrate. Reflectors for use with the Franklin slot antennas are also examined to increase the achieved directivity further.

In chapter 1, important antenna characteristics regarding antenna input and radiation performance are defined for further use in the thesis.

In chapter 2, dipole, slot, collinear and Franklin antennas are examined, as these antenna structures are fundamental to the Franklin slot antenna.

In chapter 3, analytical models for slot and Franklin slot antennas are presented. Models for the antennas with finite ground planes are purely empirical, as the ground plane truncation significantly complicates the problem. A model of a slot antenna above a flat reflector is also shown, which can be applied to the Franklin slot antenna but was not in this thesis.



In chapter 4, the Franklin slot antenna was modelled in the CST Studio Suite [6] as a thin sheet out of a perfect electric conductor (PEC) and simulated with a time domain analysis. The influence of different antenna dimensions, different amounts of radiating elements and different phasing element orientations on the antenna parameters is examined.

In chapter 5, the Franklin slot antenna was modelled in CST as a copper layer on an FR4 substrate. Antenna with and without a cutout in the FR4 substrate, different variations of metallisations, and the influence of substrate thickness, substrate permittivity and copper thickness were examined. The impact of the coaxial feed of different radii was also discussed. Four Franklin antennas for production were proposed, as well as two reflectors to use with the Franklin slot antennas.

Finally, in chapter 6, the four antennas were realised and measured. Two reflectors were also realised and measured together with Franklin slot antennas. The measured results are compared to the simulated ones.

Chapter 1

Fundamental antenna characteristics

1.1 Input characteristics

Input impedance

Input impedance is the impedance of an antenna present at its connection point. Input impedance is a frequency-dependent complex number that comprises input resistance and imaginary input reactance:

$$Z_{\text{in}}(f) = R_{\text{in}} + jX_{\text{in}} \quad (1.1)$$

Reflection coefficient

Connecting an antenna with a specific input impedance Z_{in} to a transmission line with a characteristic impedance of Z_0 creates a discontinuity that leads to reflections. This thesis only uses transmission lines with $Z_0 = 50 \Omega$. These reflections are unwanted, as they lead to a lower antenna efficiency and cause undesirable standing waves. We utilise the reflection coefficient Γ to denote the ratio of a reflected and an incident voltage wave at a discontinuity. The reflection coefficient is a complex number, and we can calculate it from input and characteristic impedances:

$$\Gamma = \frac{V^-}{V^+} = \frac{Z_{\text{in}} - Z_0}{Z_{\text{in}} + Z_0} \quad (1.2)$$

We denote the absolute value of a reflection coefficient in decibel scale as a S_{11} parameter or as a return loss RL to the negative of this value:

$$S_{11} = -RL = 20 \log |\Gamma| \quad (1.3)$$

Matching bandwidth

Because the input impedance of an antenna changes with frequency, we need to define the frequency range for which the antenna is appropriately matched to the transmission line. We refer to an antenna as well-matched for values of S_{11} of -10 dB or lower. Figure 1.1 shows a matched region of an antenna. We can calculate the matching bandwidth BW_m in % with Equation (1.4).

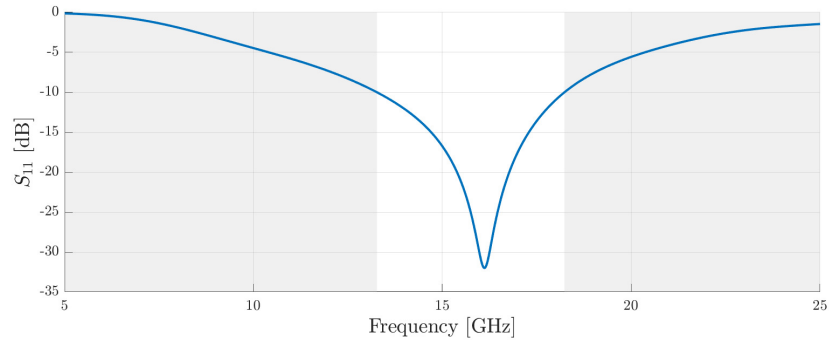


Figure 1.1: Antenna operating region with S_{11} lower than -10 dB

$$BW_m = \frac{f_{\text{high}} - f_{\text{low}}}{\frac{f_{\text{low}} + f_{\text{high}}}{2}} \cdot 100 \quad (1.4)$$

1.2 Radiation characteristics

Coordinate system

When working with antennas, we mainly use the spherical coordinate system, which can be seen in Figure 1.2, as any direction of a vector can be described only with the knowledge of elevation θ and azimuth ϕ .

Radiation intensity

Radiation intensity U is the power radiated from an antenna per unit solid angle. The radiation intensity is a far-field parameter related to the far-zone electric field of an antenna [7]. We can calculate it with [7]:

$$U(\theta, \phi) \simeq \frac{1}{2\eta} \left[\left| E_{\theta}^0(\theta, \phi) \right|^2 + \left| E_{\phi}^0(\theta, \phi) \right|^2 \right] \quad (1.5)$$

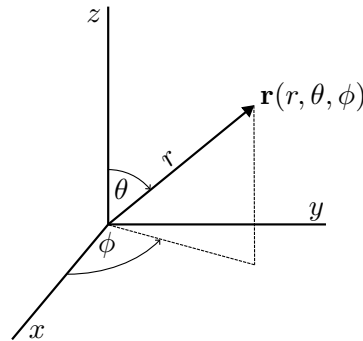


Figure 1.2: Spherical coordinates used in this thesis

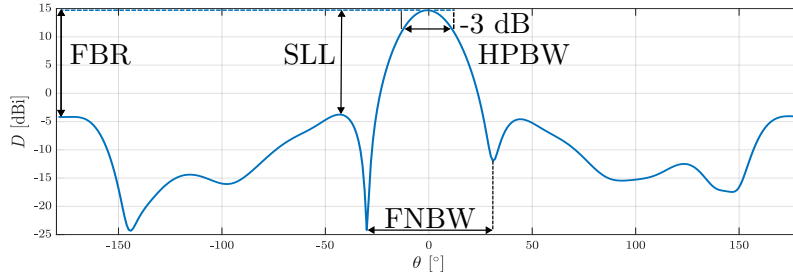


Figure 1.3: Radiation pattern with highlighted parameters

Radiation pattern

We can obtain the radiation patterns by plotting radiation intensity, directivity or gain with respect to the angular coordinates. Radiation patterns can be two or three-dimensional. In the case of a 2D radiation pattern, we plot these for the E and H planes, for which the ϕ is a constant being 90° and 0° , respectively. We can deduce multiple parameters from the radiation pattern:

- Half power beamwidth HPBW, angle for which $D \geq D_{\max} - 3$ dB
- First null beamwidth FNBW, angle for which first nulls appear
- Sidelobe level SLL, ratio between the main lobe and the sidelobes
- Front to back ratio FBR, the ratio between the front and rear directions

We can see a 2D radiation pattern with these parameters in Figure 1.3.

Polarisation

The polarisation of an antenna is the direction of the E-field in a given direction of propagation. Antenna polarisation can be either linear, circular or elliptical. In this thesis, we only examine antennas with linear polarisation. Linear polarisation has two orthogonal Ludwig 3 components. We refer to the dominant component as co-polarisation and cross-polarisation to the other.

Directivity

Directivity is the ratio of the radiation intensity in a given direction to the radiation intensity averaged over all directions [7] and can be calculated with:

$$D(\theta, \phi) = \frac{U(\theta, \phi)}{U_{\text{isotropic}}} = \frac{U(\theta, \phi)}{\frac{1}{4\pi} \int_0^{2\pi} \int_0^\pi U(\theta, \phi) \sin \theta d\theta d\phi} \quad (1.6)$$

Directivity without specified direction is usually implied as the maximum directivity of an antenna D_{\max} . Note that directivity will remain the same even if we use normalised radiation intensity instead. We usually use directivity within the decibel scale with the dBi units, for which 0 dBi is the directivity of an isotropic antenna radiating equally in all directions.

Efficiency and gain

The directivity of an antenna only considers its geometric properties, as it does not consider losses in real conductors and dielectrics. Efficiency η_{cd} of a real antenna is thus lower because of these losses. We denote gain G as a ratio between radiation intensity and accepted power that can be calculated as [7]:

$$G(\theta, \phi) = \eta_{cd}D(\theta, \phi) \quad (1.7)$$

This gain G , however, does not consider losses caused by reflections at its input. For this we introduce absolute gain G_{abs} [7]:

$$G_{abs}(\theta, \phi) = \eta_r \eta_{cd}D(\theta, \phi) = (1 - |\Gamma|)^2 G(\theta, \phi) \quad (1.8)$$

Effective aperture

Effective aperture A_{eff} is defined as an area of an antenna, which outputs the same amount of power at its terminals as it intercepts [8]. Effective aperture is related to the directivity and wavelength as it is the minimum aperture size of an antenna with a given directivity at a specific wavelength.

$$A_{eff} = \frac{\lambda^2}{4\pi} D \quad (1.9)$$

Aperture efficiency $\eta_{aperture}$ is the ratio between the effective and physical aperture size. It normally ranges from 50 to 80 % [9].

$$\eta_{aperture} = \frac{A_{eff}}{A_{phys}} \quad (1.10)$$

Radiation bandwidth

We can define the radiation bandwidth BW_r similarly to the BW_m since the radiation pattern and, thus, the directivity within the desired direction are frequency-dependent as well. We consider 3 dB as a maximum acceptable decrease in directivity from its maximum, as shown in Figure 1.4. Radiation bandwidth can be calculated similarly with Equation (1.4).

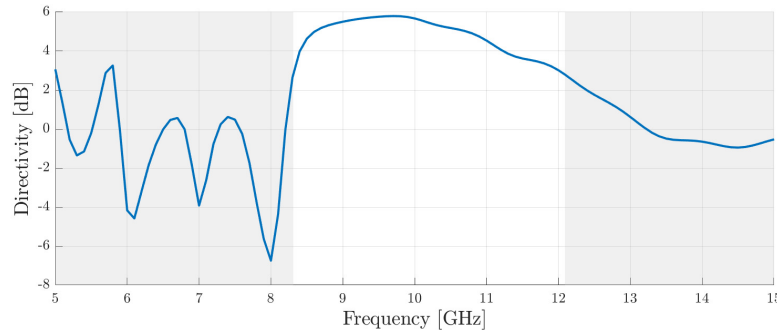


Figure 1.4: Antenna operating region with less than 3 dB decrease of directivity

Chapter 2

Commonly used antenna structures

2.1 Electric dipole

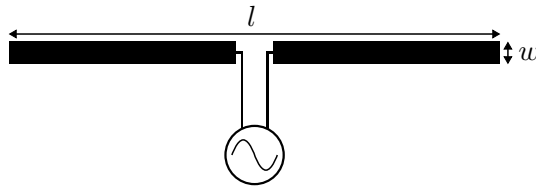


Figure 2.1: Dipole antenna

The electric dipole antenna is one of the most commonly used antenna structures. This type of antenna comprises two radiating elements placed lengthwise next to each other, fed by a voltage source from the middle. Such an antenna has dimensions l and w , where l is the length of both radiating elements, and w is their width, as shown in Figure 2.1. Dipole antennas usually have length l much larger than width w . For these thin antennas, we can assume that the width is negligible and Equation 2.1 serves as a decent approximation of its current distribution [7]:

$$I(z) = \begin{cases} I_0 \sin \left[k \left(\frac{l}{2} - z \right) \right], & 0 \leq z \leq \frac{l}{2} \\ I_0 \sin \left[k \left(\frac{l}{2} + z \right) \right], & -\frac{l}{2} \leq z \leq 0 \end{cases} \quad (2.1)$$

where I is current distribution along the z axis, I_0 is current amplitude and k is wave number. Radiation intensity was derived from this current distribution in [7] as:

$$U(\theta) = \eta \frac{|I_0|^2}{8\pi^2} \left[\frac{\cos \left(\frac{kl}{2} \cos \theta \right) - \cos \left(\frac{kl}{2} \right)}{\sin \theta} \right]^2 \quad (2.2)$$

Because dipole antennas are rotationally symmetric in the xy plane, the radiation intensity depends only on θ , and its radiation pattern is omnidirectional in the H plane. The shape of the normalised radiation pattern will only depend on the antenna's electrical length kl . We typically describe dipole length as a multiple of wavelength λ at dipole operating frequency.

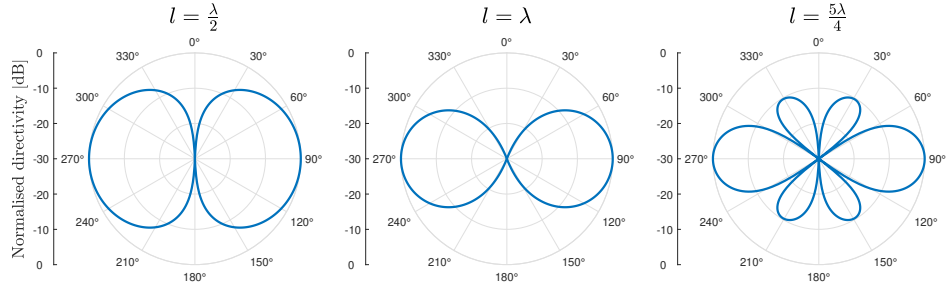


Figure 2.2: Radiation pattern in E plane for different dipole lengths

Figure 2.2 shows radiation patterns for different dipole lengths. As the length of the dipole increases, the beamwidth of the main lobe decreases, and additional sidelobes start appearing for λ greater than 1. Directivity tends to increase with increasing λ ; however, after $l = \frac{5\lambda}{4}$, sidelobes become more prevalent. We can find directivity dependence on dipole length in [7].

In practice, the most used length of a dipole antenna is $l = \frac{\lambda}{2}$. We call dipoles with this length the half-wavelength dipoles. The input impedance of a half-wavelength dipole is well-matched to both 50Ω and 75Ω transmission lines since $Z_{in} = 73 + j42.5\Omega$ as it was shown in [7]. In Figure 2.3, we can see that for the half-wavelength dipole, its impedance is unaffected by its width w . We can see the radiation pattern of a half-wavelength dipole in Figure 2. The half-wavelength antenna is omnidirectional in the H plane as any other dipole, and it is bidirectional in the E plane with a rather large HPBW of 78° . The directivity of the half-wavelength dipole is 2.15 dBi.

The dipole antenna was modelled as two thin rectangles with PEC of overall length $l = 15$ mm and width w in CST. This antenna is a half-wavelength dipole for an operating frequency of 10 GHz. We simulated this antenna for multiple values of w to find the dependence of input impedance on its width. Figure 2.3 shows that antennas with smaller widths tend to have steeper resistance and reactance values, except for l being $\frac{\lambda}{2}$. We can also see that dipole antennas are in resonance for l slightly smaller than $\frac{\lambda}{2}$.

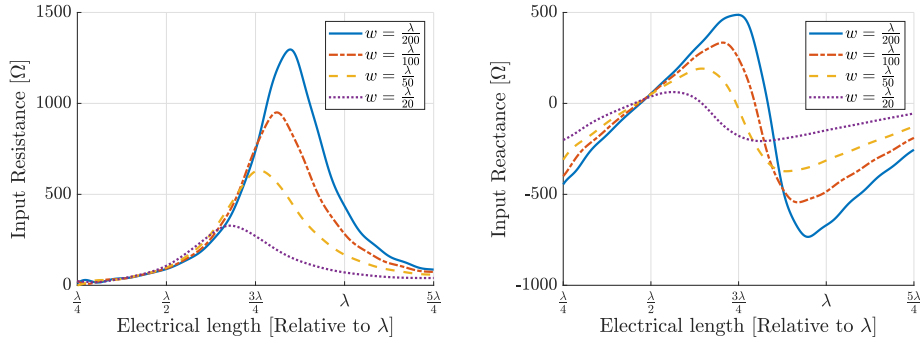


Figure 2.3: Dipole input resistance and reactance for different values of w

2.2 Slot antenna

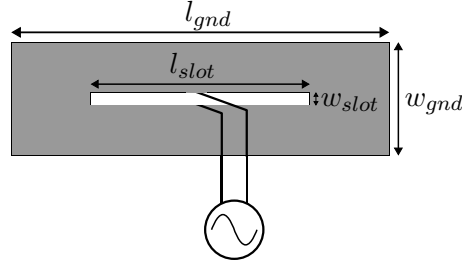


Figure 2.4: Slot antenna

Slot antennas are prevalent antenna structures that come in many forms. These antennas take the shape of a conductive screen with a slot cutout fed by a current source. The shape of the slot cutout and screen can be arbitrary; however, here, we will only consider a slot cutout of a rectangular shape with length l_{slot} and width w_{slot} in a rectangular screen with length l_{gnd} and width w_{gnd} . We can see such an antenna in Figure 2.4.

Consider a slot antenna with an infinite screen and slot cutout dimensions such that $l_{\text{slot}} \gg w_{\text{slot}}$. An electric field perpendicular to the length l_{slot} is excited inside the slot as the antenna gets fed. We can now use the field equivalence principle, which represents actual radiating sources on an enclosed surface as fictitious electric and magnetic currents through the following equations [9]:

$$\mathbf{J}_S = \hat{\mathbf{n}} \times \mathbf{H} \quad (2.3)$$

$$\mathbf{M}_S = -\hat{\mathbf{n}} \times \mathbf{E} \quad (2.4)$$

In our case, we evaluate tangential fields over the surface of our slot antenna. Our surface comprises an electric conductor with a slot cutout, which we can approximate as infinitesimally thin. Only \mathbf{M}_S is relevant since $\mathbf{H} = 0$ over the entire surface. Tangential \mathbf{E} field will be only present inside the slot cutout. By using Equation 2.3, we can substitute this field with a fictional magnetic current \mathbf{M}_S present inside the slot that is perpendicular to both the antenna surface and the direction of the \mathbf{E} field. The magnetic current distribution that will be excited is similar to one for the electric dipole in Equation 2.1. We have thus shown that this slot antenna behaves as a thin magnetic dipole of length l_{slot} through the equivalence principle [9].

Electric dipole	Magnetic dipole
Fed by a voltage source	Fed by a current source
\mathbf{J}	\mathbf{M}
\mathbf{E}_1	\mathbf{H}_2
\mathbf{H}_1	$-\mathbf{E}_2$

Table 2.1: Properties of electric and magnetic dipoles as linked through duality

Using the duality principle, we can equate the fields of an electric dipole to the fields of a magnetic dipole of the same length, as shown in Table 2.1 [9]. Since values of the normalised fields \mathbf{E}_θ and \mathbf{H}_ϕ of an electric dipole are equal, as we apply the duality principle, these normalised fields get replaced by \mathbf{E}_ϕ and \mathbf{H}_θ for the magnetic dipole respectively [9]. This interchange does not affect the radiation pattern, only the polarisation. This derivation of the radiation pattern only applies to slot antennas of infinite dimensions; radiation patterns for slot antennas get reviewed in more depth in chapter 3.

We can obtain the input impedance for the slot antenna through Babinet's principle. Babinet's principle is mainly used in optics; however, a unique formulation exists for antennas [9]. As shown in Equation 2.5, this formulation equates an antenna's impedance to the impedance of a complementary-shaped antenna. An antenna is complementary to another antenna if both shapes when added together, cover the entire plane and do not overlap each other. In this interpretation, the impedance of a slot antenna is indirectly proportional to the impedance of a complementary dipole.

$$Z_{\text{original}} Z_{\text{complementary}} = \frac{(120\pi)^2}{4} \quad (2.5)$$

The slot antenna was modelled as a rectangle with length l_{gnd} of 17 mm and width w_{gnd} of 12 mm with a rectangular slot cutout of length l_{slot} of 15 mm and width w_{slot} in CST. We simulated this antenna for multiple values of w_{slot} to show its behaviour based on different widths of the slot. Figure 2.5 shows the simulated impedance and reflection coefficient.

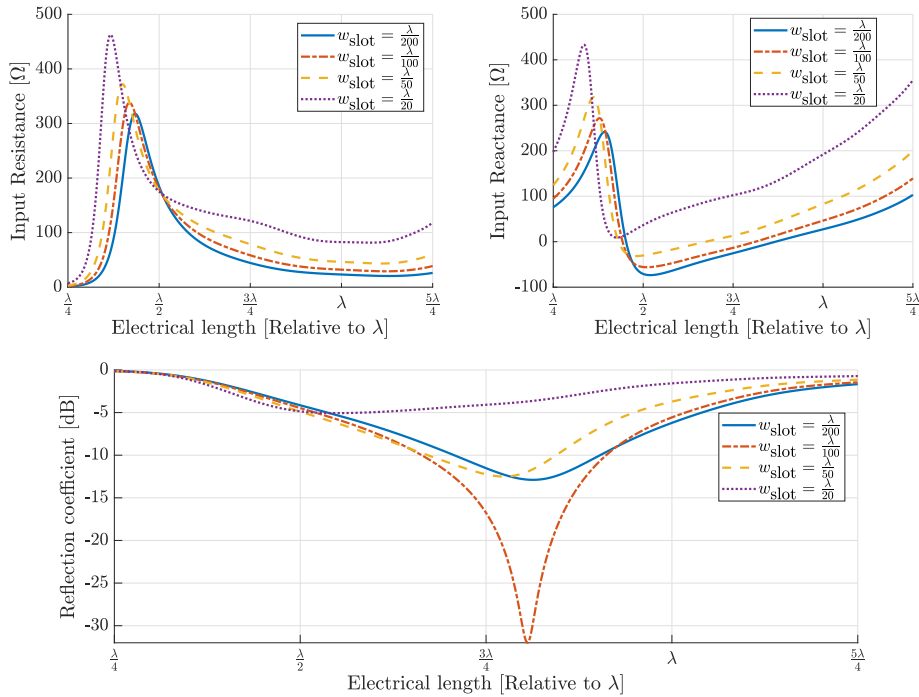


Figure 2.5: Slot antenna input characteristics for different values of w_{slot}

Because of Babinet's principle, resonances of the electric dipole become antiresonances for the slot antenna and vice versa. Slot antennas with slot length $l_{\text{slot}} = \frac{\lambda}{2}$ are matched quite poorly because of the near antiresonance. However, they can be matched very well for $l_{\text{slot}} = \frac{3\lambda}{4}$ since slot width w_{slot} affects the impedance in this region, as Figure 2.5 shows. Slot antennas can thus achieve superior bandwidth to dipole antennas. We should choose the dimensions of the ground plane carefully, as a larger ground plane size can lead to unstable radiation for higher frequencies [1] and length l_{gnd} affects antenna impedance.

2.3 Antenna array

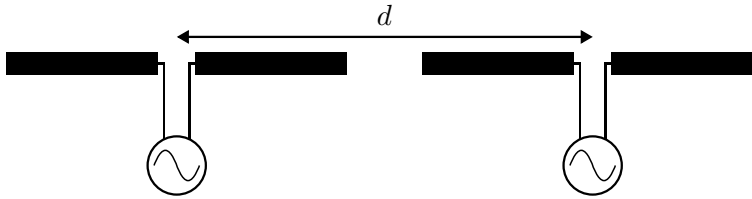


Figure 2.6: Antenna array formed by two dipoles

By using multiple radiating elements, we can form an antenna array. Antenna arrays are widely utilised for their high directivity, relative simplicity and even the possibility of a steerable beam. Antenna arrays usually consist of multiple identical radiating elements placed at different points in space. Figure 2.6 shows two dipoles placed lengthwise next to each other, with their origins spaced by distance d . These dipoles thus form a simple antenna array of two elements positioned on a singular axis.

Suppose we know the radiation pattern of a singular dipole. In that case, we can obtain the radiation pattern of an antenna array composed of these identical dipoles using the array multiplication principle [8]:

$$U_{\text{array}}(\theta, \phi) = |A(\theta, \phi)|^2 U_{\text{dipole}}(\theta, \phi) \quad (2.6)$$

The radiation intensity of an antenna array is a product of the radiation intensity of a single radiating element and the square of the absolute value of an antenna array factor A . Array factor A thus encapsulates the positioning as well as feeding. We can obtain the array factor with the following Equation [8]:

$$A(\hat{\mathbf{r}}) = \sum_{n=1}^N a_n e^{jk\hat{\mathbf{r}} \cdot \mathbf{d}_n} \quad (2.7)$$

where N represents the number of elements, a_n is the n th feed coefficient, k is the wave number, $\hat{\mathbf{r}}$ is the normalised wave vector, and \mathbf{d}_n is a vector of the n th element position. The antenna array factor $A(\hat{\mathbf{r}})$ thus represents the sum of individual translational phase shifts in a given direction for each element. Note that the feeding coefficient a_n is a complex number; its amplitude describes the signal's amplitude relative to amplitudes of other feeding signals, and its angle describes the signal's relative phase at the feed.

For arrays with radiating elements placed only along a single axis, we can simplify Equation (2.7) since only one component will stay relevant after the dot product. It is preferable to choose the z-axis, as the transformation to spherical coordinates will be independent of ϕ as seen here [8]:

$$A(\theta) = \sum_{n=1}^N a_n e^{jk d_n \cos \theta} \quad (2.8)$$

Look at the two half-wavelength dipoles in Figure 2.6. This particular setup, with the dipoles arranged lengthwise, is known as a collinear array. In this case, we feed the dipole antennas with two signals of the same amplitude and phase, thus $a_1 = 1$ and $a_1 = 1$. The dipoles are positioned at $\pm \frac{d}{2}$ from the centre. We can now use (2.8) to find an array factor for this configuration [7]:

$$A(\theta) = e^{jk \frac{d}{2} \cos \theta} + e^{-jk \frac{d}{2} \cos \theta} = 2 \cos \left(\frac{kd}{2} \cos \theta \right) \quad (2.9)$$

where we have used the cosine exponential form to rewrite the two exponentials. If we use the normalised version of (2.2) and (2.9) according to the array multiplication principle (2.6), we can obtain the normalised radiation intensity of the array. This collinear array retains the omnidirectionality of a single dipole in the H plane. The main beam in the E-plane is narrower, and the antenna array has an increased directivity than a single element. Radiation pattern and directivity depend on the spacing of elements d as shown in Figure 2.7. We can achieve the maximum directivity with a spacing of λ , after which the sidelobes become more prevalent, and the directivity starts to drop.

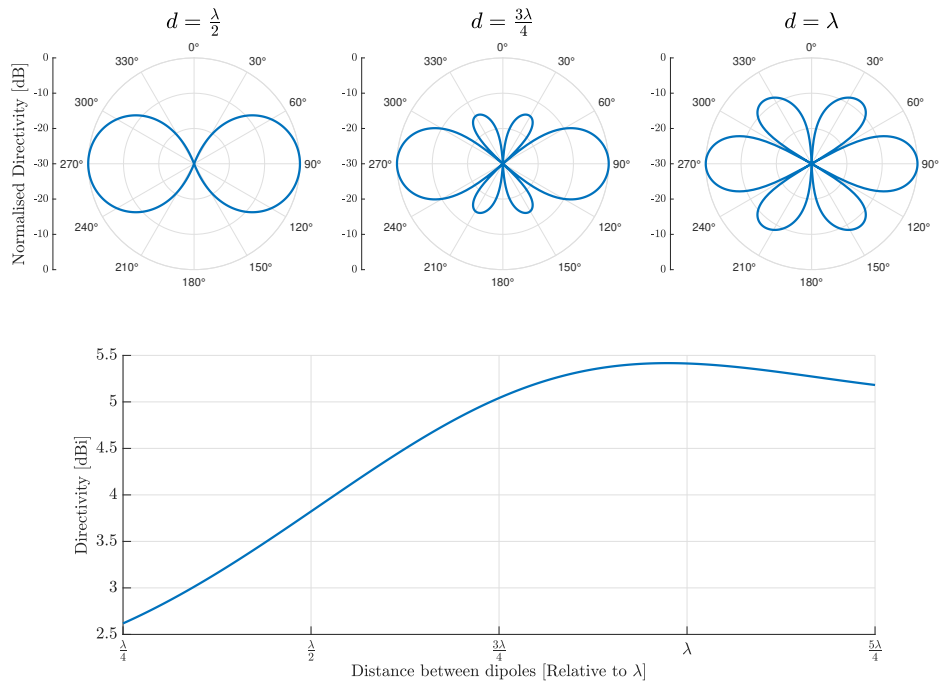


Figure 2.7: Radiation characteristics of two half-wavelength dipoles

2.4 Franklin antenna

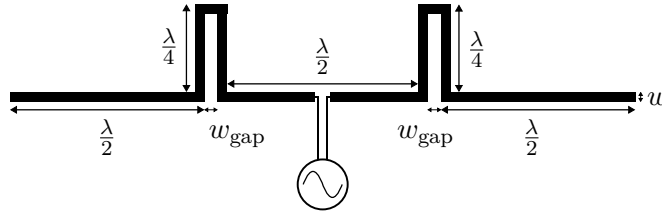


Figure 2.8: Three-element Franklin antenna

As the previous section shows, we can stack dipoles fed in phase lengthwise to achieve higher directivity. For simplicity, we desire to join these elements electrically to feed the antenna with a single source. However, if we recall the Equation for dipole current distribution (2.1), we know that for dipoles longer than $\frac{\lambda}{2}$, the current will have the opposite direction than the current at the feed point in some sections. Franklin antenna, as discovered by C. S. Franklin in 1924 [2], deals with these opposite currents by utilising U-shaped sections, where the fields caused by the opposite currents cancel out. Figure 2.8 displays a Franklin antenna featuring three radiating elements. Such an antenna has three half-wavelength radiating elements placed horizontally and two phasing elements bent in the U-shape with the height of $\frac{\lambda}{4}$ separated by a gap of width w_{gap} , with all elements having a width w .

These horizontal elements thus form a collinear array and are spaced by a distance d of $\frac{\lambda}{2} + w_{\text{gap}}$. Since the width of the gap should be small because of the phasing elements, the spacing will be around 0.55λ to 0.7λ . Figure 2.7 shows that this spacing leads to a smaller directivity gain than possible. Adding more horizontal radiating elements to a Franklin antenna will increase its directivity, which we can approximate as (modified equation from [10]):

$$D_{\text{dB}} = 2.15 + 0.7 \cdot 10 \log N \quad (2.10)$$

where the N represents the number of elements, 2.15 dBi is the directivity of a single radiating element, and 0.7 is a coefficient representing the spacing of the dipoles $d = 0.6\lambda$. Franklin antennas typically have an odd number of radiating elements, with the centermost one fed like a regular dipole. The directivity for different numbers of horizontal elements N is shown in Table 2.2. We can see that the directivity yield gets smaller with more radiating elements. The directivity of a Franklin antenna is also sensitive to deviations from the operating frequency, as the changing current distribution will no longer match the position of radiating and phased elements. A three-element Franklin antenna is directive in the main direction from $0.85f$ to $1.15f$, where f is the frequency for which the radiating elements are $\frac{\lambda}{2}$ long.

Number of elements	1	2	3	5	7	9	11
Directivity [dBi]	2.15	4.25	5.49	7.04	8.07	8.82	9.44

Table 2.2: Approximate directivity of a Franklin antenna with N elements

The Franklin antenna was modelled with the length of radiating elements of 15 mm, height of phasing elements of 7.5 mm and gap inside the phasing element w_{gap} of 2 mm in CST. The operating frequency for this antenna is 10 GHz. We have first simulated the Franklin antenna for three, five and seven radiating elements with a width w of 0.3 mm. Figure 2.9 shows the radiation patterns for these antennas at their operating frequency. The main beam gets narrower with a higher number of elements N . Due to the phasing elements being all on one side, the radiating pattern is slightly asymmetrical. This asymmetry is very noticeable in the H-plane, which is not displayed, where the radiation pattern is no longer independent of theta, as was the case for the dipole. However, the difference is less than -3 dB; thus, it can still be considered omnidirectional. We can reduce this effect by making the Franklin antenna diagonally symmetrical; we can achieve this for a three-element Franklin antenna by flipping one of the phasing elements around. More than one diagonally symmetrical variation of flipped elements exists for antennas with more than three elements.

We have also simulated the three-element Franklin antenna for different width values w . Figure 2.10 shows the input impedance for this antenna. When we compare this input impedance to the input impedance of a dipole shown in Figure 2.3, we can see more resonances and antiresonances present. The smaller widths, again, tend to have steeper resonance and reactance values. This time, the impedance depends on w in the $\frac{\lambda}{2}$ region.

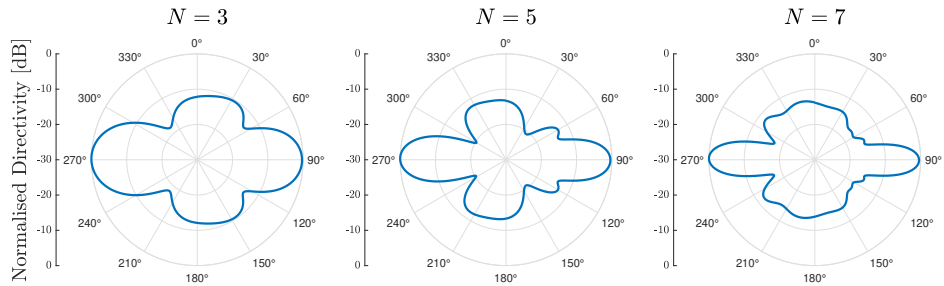


Figure 2.9: Radiation characteristics of Franklin antennas with N elements

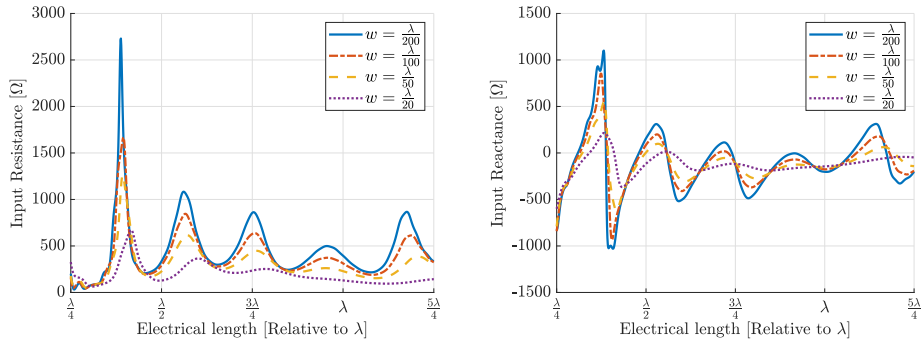


Figure 2.10: Three-element Franklin antenna input impedance for different values of w

Chapter 3

Theoretical models for slot antennas

3.1 Slot antenna as an aperture

In section 2.2, we have shown that slot antenna with a rectangular cutout of length l_{slot} and infinitesimal width w_{slot} on infinite ground plane behaves like a magnetic dipole. Its radiation pattern is thus the same as one of an electric dipole of length $l = l_{\text{slot}}$. In this section, we will view the slot antenna as an aperture of length $a = l_{\text{slot}}$ and width $b = w_{\text{slot}}$ on an infinite ground plane once again. We can find the following equations used in this section in [7], where a similar problem for unidirectional apertures was evaluated.

Square aperture with uniform distribution

Let us consider a uniform distribution of E-field perpendicular to length l_{slot} on our aperture as shown in Figure 3.1. In this case, the following equation represents the tangential E-field present on the aperture:

$$\mathbf{E}_a = \begin{cases} \hat{\mathbf{y}}E_0, & \text{for } -\frac{a}{2} \leq x' \leq \frac{a}{2} \text{ and } -\frac{b}{2} \leq y' \leq \frac{b}{2} \\ \mathbf{0}, & \text{everywhere else} \end{cases} \quad (3.1)$$

We can now evaluate the equivalent magnetic and electric currents \mathbf{M}_s and \mathbf{J}_s present on the surface of the aperture with the equations (2.3) and (2.4). Since no tangential H-field is present on the aperture, only the magnetic current \mathbf{M}_s is relevant. The following equations describe these currents:

$$\mathbf{M}_s = \begin{cases} \hat{\mathbf{x}}E_0, & \text{for } -\frac{a}{2} \leq x' \leq \frac{a}{2} \text{ and } -\frac{b}{2} \leq y' \leq \frac{b}{2} \\ \mathbf{0}, & \text{everywhere else} \end{cases} \quad (3.2)$$

$$\mathbf{J}_s = \mathbf{0}, \quad \text{everywhere} \quad (3.3)$$

In [7], the magnetic current \mathbf{M}_s is instead equal to $\hat{\mathbf{x}}2E_0$ on the aperture because aperture in problem from [7] radiates only unidirectionally. The aperture is thus treated as an electric conductor, and by exciting a magnetic current on one side of the aperture, another current with the same direction will appear on the other side due to the image theory. Due to the proximity, these currents add together, and \mathbf{M}_s for their problem is doubled.

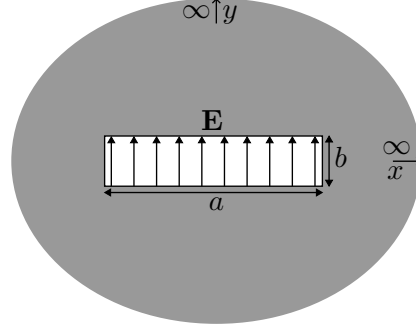


Figure 3.1: Aperture on an infinite ground plane with uniform E-field distribution

To obtain the radiated E and H fields by the aperture, we would now need to get the \mathbf{A} and \mathbf{F} potentials from \mathbf{J}_s and \mathbf{M}_s respectively. We will instead only consider the far-field approximation \mathbf{L} of the \mathbf{F} potential decomposed into L_θ and L_ϕ . Equations for L_θ and L_ϕ with only M_x being nonzero are [7]:

$$L_\theta = \cos \theta \cos \phi \left[\int_{-\frac{b}{2}}^{\frac{b}{2}} \int_{-\frac{a}{2}}^{\frac{a}{2}} M_x e^{jk(x' \sin \theta \cos \phi + y' \sin \theta \sin \phi)} dx' dy' \right] \quad (3.4)$$

$$L_\phi = \sin \phi \left[\int_{-\frac{b}{2}}^{\frac{b}{2}} \int_{-\frac{a}{2}}^{\frac{a}{2}} M_x e^{jk(x' \sin \theta \cos \phi + y' \sin \theta \sin \phi)} dx' dy' \right] \quad (3.5)$$

We can now plug in M_x from Equation (3.2) into the equation from above:

$$L_\theta = E_0 \cos \theta \cos \phi \left[\int_{-\frac{b}{2}}^{\frac{b}{2}} \int_{-\frac{a}{2}}^{\frac{a}{2}} e^{jk(x' \sin \theta \cos \phi + y' \sin \theta \sin \phi)} dx' dy' \right] \quad (3.6)$$

$$L_\phi = E_0 \sin \phi \left[\int_{-\frac{b}{2}}^{\frac{b}{2}} \int_{-\frac{a}{2}}^{\frac{a}{2}} e^{jk(x' \sin \theta \cos \phi + y' \sin \theta \sin \phi)} dx' dy' \right] \quad (3.7)$$

The integral from the equation from above is evaluated in [7] and leads to the following solution for L_θ and L_ϕ :

$$L_\theta = abE_0 \left[\cos \theta \cos \phi \left(\frac{\sin X}{X} \right) \left(\frac{\sin Y}{Y} \right) \right] \quad (3.8)$$

$$L_\phi = -abE_0 \left[\sin \phi \left(\frac{\sin X}{X} \right) \left(\frac{\sin Y}{Y} \right) \right] \quad (3.9)$$

Both L_θ and L_ϕ are functions of θ and ϕ and depend on E-field magnitude E_0 , wave number k , length a and width b of the aperture. X and Y in the equations above represent the following equations:

$$X = \frac{ka}{2} \sin \theta \cos \phi \quad (3.10)$$

$$Y = \frac{kb}{2} \sin \theta \sin \phi \quad (3.11)$$

We can now easily obtain E and H far-fields from equations (3.8) and (3.9) as shown in [7]. Note that these fields are only valid in the far-field region

($r \gg \frac{\lambda}{2\pi}$) because of the approximation used. The E and H fields are:

$$E_\theta = j \frac{abkE_0 e^{-jkr}}{4\pi r} \left[\sin \phi \left(\frac{\sin X}{X} \right) \left(\frac{\sin Y}{Y} \right) \right] \quad (3.12)$$

$$E_\phi = j \frac{abkE_0 e^{-jkr}}{4\pi r} \left[\cos \theta \cos \phi \left(\frac{\sin X}{X} \right) \left(\frac{\sin Y}{Y} \right) \right] \quad (3.13)$$

$$H_\theta = -\frac{E_\phi}{\eta} \quad (3.14)$$

$$H_\phi = \frac{E_\theta}{\eta} \quad (3.15)$$

We can now make the E-field independent of r for the use in Equation (1.6), which we utilize to calculate radiation intensity $U(\theta, \phi)$:

$$E_\theta^0 = C \left[\sin \phi \left(\frac{\sin X}{X} \right) \left(\frac{\sin Y}{Y} \right) \right] \quad (3.16)$$

$$E_\phi^0 = C \left[\cos \theta \cos \phi \left(\frac{\sin X}{X} \right) \left(\frac{\sin Y}{Y} \right) \right] \quad (3.17)$$

Where C in the equation above represents:

$$C = j \frac{abkE_0}{4\pi} \quad (3.18)$$

The following E-fields, we acquired in equations (3.16) and (3.17), require us to provide a length of our slot aperture a , its width b , and the wave number k tied to the operating frequency. They also require an antenna constant C defined in Equation (3.18); however, we can neglect this constant if we wish to calculate the normalised radiation intensity. The normalisation affects only the scaling of the radiation pattern, not the shape, so Equation (1.6) for directivity will provide the same results regardless. Note that this approximation regards only the co-polarisation as the cross-polarisation is zero for this model. We have calculated this model for a slot antenna with aperture dimensions $a = 15$ mm and $b = 0.7$ mm operating at 10 GHz. Figure 3.2 shows the results for this model; we can see that the antenna is omnidirectional in the E-plane, and its pattern is similar to the dipole one.

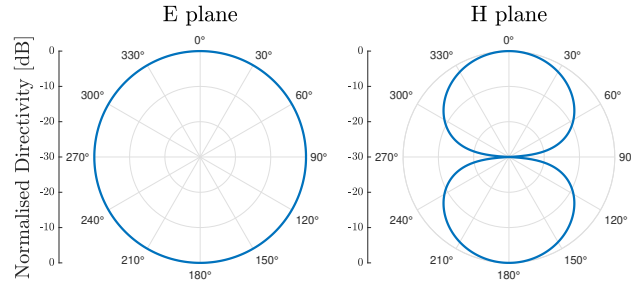


Figure 3.2: Radiation pattern for slot antenna with uniform E-field distribution

■ Square aperture with cosine distribution

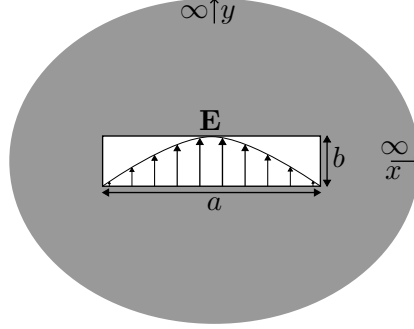


Figure 3.3: Aperture on an infinite ground plane with cosine E-field distribution

Let us now consider a similar problem with the cosine distribution of the E-field instead. In Figure 3.3, we can see an aperture with the cosine distribution. The following equation describes the tangential E-field with the half-wave cosine distribution on the aperture [7]:

$$\mathbf{E}_a = \begin{cases} \hat{\mathbf{y}}E_0 \cos\left(\frac{\pi}{a}x'\right), & \text{for } -\frac{a}{2} \leq x' \leq \frac{a}{2} \text{ and } -\frac{b}{2} \leq y' \leq \frac{b}{2} \\ \mathbf{0}, & \text{everywhere else.} \end{cases} \quad (3.19)$$

We can once again obtain the equivalent field sources for this variation:

$$\mathbf{M}_s = \begin{cases} \hat{\mathbf{x}}E_0 \cos\left(\frac{\pi}{a}x'\right), & \text{for } -\frac{a}{2} \leq x' \leq \frac{a}{2} \text{ and } -\frac{b}{2} \leq y' \leq \frac{b}{2} \\ \mathbf{0}, & \text{everywhere else.} \end{cases} \quad (3.20)$$

$$\mathbf{J}_s = \mathbf{0}, \quad \text{everywhere} \quad (3.21)$$

By plugging the \mathbf{M}_s into the equations (3.8) and (3.9), we can once again obtain L_θ and L_ϕ far-field potential approximations for the variation with the cosine distribution. Since E_0 is the constant, we can factor it from the integral; however, we will have to evaluate the integral with the cosine distribution function, as it is a function of x' .

$$L_\theta = E_0 \cos \theta \cos \phi \left[\int_{-\frac{b}{2}}^{\frac{b}{2}} \int_{-\frac{a}{2}}^{\frac{a}{2}} \cos\left(\frac{\pi}{a}x'\right) e^{jk(x' \sin \theta \cos \phi + y' \sin \theta \sin \phi)} dx' dy' \right] \quad (3.22)$$

$$L_\phi = E_0 \sin \phi \left[\int_{-\frac{b}{2}}^{\frac{b}{2}} \int_{-\frac{a}{2}}^{\frac{a}{2}} \cos\left(\frac{\pi}{a}x'\right) e^{jk(x' \sin \theta \cos \phi + y' \sin \theta \sin \phi)} dx' dy' \right] \quad (3.23)$$

The integrated solution for these L_θ and L_ϕ can be found in [7] and is shown in the following equations. We can see that these L_θ and L_ϕ for the cosine distribution are similar to the ones with uniform distribution.

$$L_\theta = -\frac{\pi}{2} ab E_0 \left[\cos \theta \cos \phi \left(\frac{\cos X}{X^2 - \left(\frac{\pi}{2}\right)^2} \right) \left(\frac{\sin Y}{Y} \right) \right] \quad (3.24)$$

$$L_\phi = \frac{\pi}{2} ab E_0 \left[\sin \phi \left(\frac{\cos X}{X^2 - \left(\frac{\pi}{2}\right)^2} \right) \left(\frac{\sin Y}{Y} \right) \right] \quad (3.25)$$

The X and Y are once again represented by the equations (3.10) and (3.11). We can see that the $\frac{\sin Y}{Y}$ for L_θ and L_ϕ is the present for both versions; however X dependence is different, the signs for L_θ and L_ϕ are swapped and a $\frac{\pi}{2}$ constant is present for the uniform distribution. We can once again calculate far-field approximations of the E and H fields from L_θ and L_ϕ [7]:

$$E_\theta = j \frac{abkE_0e^{-jkr}}{8r} \left[\sin \phi \left(\frac{\cos X}{X^2 - (\frac{\pi}{2})^2} \right) \left(\frac{\sin Y}{Y} \right) \right] \quad (3.26)$$

$$E_\phi = j \frac{abkE_0e^{-jkr}}{8r} \left[\cos \theta \cos \phi \left(\frac{\cos X}{X^2 - (\frac{\pi}{2})^2} \right) \left(\frac{\sin Y}{Y} \right) \right] \quad (3.27)$$

$$H_\theta = -\frac{E_\phi}{\eta} \quad (3.28)$$

$$H_\phi = \frac{E_\theta}{\eta} \quad (3.29)$$

Same as before, we can now make the E-field independent of r and obtain:

$$E_\theta^0 = -\frac{\pi}{2} C \left[\sin \phi \left(\frac{\cos X}{X^2 - (\frac{\pi}{2})^2} \right) \left(\frac{\sin Y}{Y} \right) \right] \quad (3.30)$$

$$E_\phi^0 = -\frac{\pi}{2} C \left[\cos \theta \cos \phi \left(\frac{\cos X}{X^2 - (\frac{\pi}{2})^2} \right) \left(\frac{\sin Y}{Y} \right) \right] \quad (3.31)$$

The constant C is the same for this variation as for the previous one from Equation (3.18); however, a $-\frac{\pi}{2}$ constant has now appeared next to C for the cosine distribution model. If we wish to calculate only the normalised U , we can again disregard both constants. We once again need to provide these equations (3.30) and (3.31) with the antenna values of a , b and k . This model only considers co-polar directivity. Again, we calculated this model for a slot antenna with aperture dimensions $a = 15$ mm and $b = 0.7$ mm operating at 10 GHz. Figure 3.4 shows the results for the model with cosine distribution; we can see that the radiation pattern is similar to the model with uniform distribution. In the E-plane, the radiation pattern is once again omnidirectional. In the H-plane, the radiation pattern for cosine distribution resembles $\frac{\lambda}{2}$ dipole pattern from Figure 2.2 even closer.

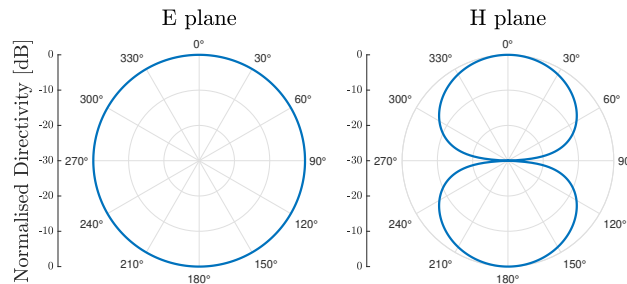


Figure 3.4: Radiation pattern for slot antenna with cosine E-field distribution

3.2 Effects of finite ground plane

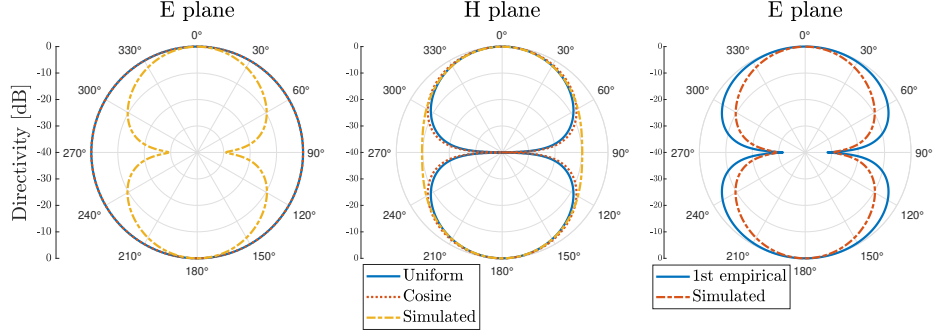


Figure 3.5: Comparison between analytical and simulated models of slot antennas

The previous model from section 3.1 only applies to the slot antennas with infinite ground planes. Real slot antennas will always have ground planes of a finite length l_{gnd} and width w_{gnd} . This truncation of the ground plane significantly affects the slot antenna radiation patterns. We have simulated a slot antenna with the exact slot dimensions as for infinite ground plane models from section 3.1 with the ground plane dimensions l_{gnd} and w_{gnd} being 25 mm. The first two plots in Figure 3.5 compare the radiation pattern of the simulated slot antenna to the models from 3.1. We can see that the finite slot antenna is bidirectional in the E-plane instead.

Finding an analytical model for the slot antenna is much more complicated, as there are now E and H fields in the antenna plane outside the slot itself. This problem is approached in literature as a diffraction problem in the E-plane [7], [11]. Only the E-plane is considered as the E-field magnitude on the edges of the slot in the H-plane is zero [11]. The uniform theory of diffraction [11] or geometrical theory of diffraction [7] is then applied to the problem. These models are complicated and only affect the E-plane radiation pattern as they only consider wedge diffraction. There is also significant vertex diffraction that is not accounted for in these models [11].

Instead, we will empirically model the slot antenna with the finite ground plane. One of these empirical models is shown in [12] as:

$$E(\theta, \phi = 90^\circ) = \sqrt{1 + 4b \cos(\beta d \cos(\beta d \sin \theta))} \quad (3.32)$$

In this equation, β is the phase constant tied to the antenna frequency, d is the distance between the centre of the aperture and the antenna edge in the E-plane, and b is the amplitude constant representing the edge radiation. Constant b is to be chosen empirically in this case. The third plot in Figure 3.5 compares this model and the simulated one. Only the E-plane is plotted, as this equation only considers this plane.

We will, however, consider a different model because the previous one is limited by being only in the E-plane. Notice that the H-field of the uniform distribution model in Figure 3.5 represents both the simulated E and H

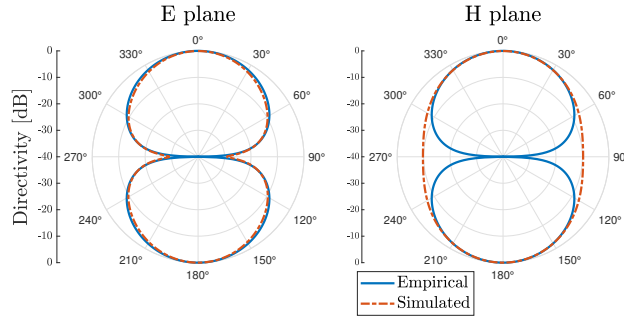


Figure 3.6: Uniform empirical H-pattern model for both planes

patterns pretty well for a beamwidth of 90° . We will thus model the slot antenna with the uniform distribution H-pattern for all directions. We can obtain the equation for by simply plugging $\phi = 0$ into Equation (3.17):

$$E(\theta) = C \cos \theta \left(\frac{\sin X_\theta}{X_\theta} \right); \quad X_\theta = \frac{ka}{2} \sin \theta \quad (3.33)$$

In Figure 3.6, we can see that for angles greater than $\pm 45^\circ$, the radiation intensity for our model drops compared to the simulated results. We can address this by introducing a correcting empirical factor, as shown here:

$$U(\theta, \phi) = |E(\theta)|^2 + |C(\sqrt{A} \cos \phi + \sqrt{B} \sin \phi)|^2 \quad (3.34)$$

In this equation, the A and B are empirical constants representing the minimum linear radiation intensity values in the H and E planes. The first two plots in Figure 3.7 compare this model and a simulated one in the E and H planes. We can see that these radiation patterns align well. Since this empirical model can produce three-dimensional radiation patterns, we can utilise Equation (1.6) to calculate the antenna's directivity. The calculated directivity obtained from this model is 5.7 dBi, while it is 5.3 dBi for the simulated one. The difference is mainly due to the higher radiation intensity for the directions of the antenna vertices. We can see the influence of these vertices in Figure 3.7, where the normalised directivity $D(\theta = 90^\circ, \phi)$ is shown.

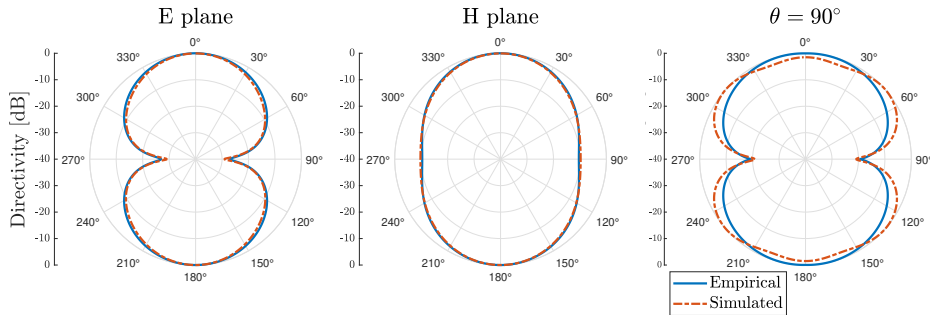


Figure 3.7: Uniform empirical model with correction

3.3 Slot antenna with a reflector

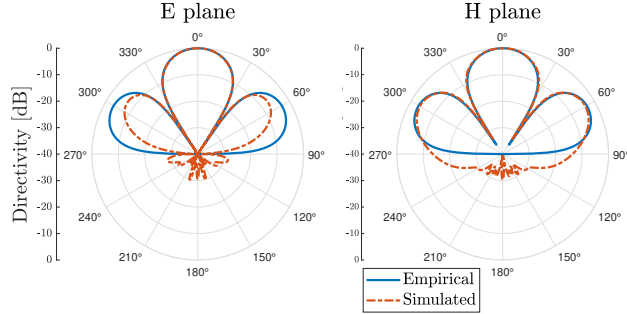


Figure 3.8: Simple model with a flat reflector

Let us now consider a slot antenna above an electrically conductive ground plane. This problem requires the use of image theory, which transforms it into a situation where an antenna image is created on the opposite side of the ground plane to account for it [7]. For our configuration, the image will be in phase, and the problem leads to the following equation [7]:

$$U(\theta, \phi) = |E(\theta)2 \cos(k(0.5h) \cos \theta)|^2 \quad (3.35)$$

In this equation, k is the wave number, and h is the distance between the antenna and reflector. In [7], only h is present instead of $0.5h$; however, this gives wrong results in our case for an unknown reason. We can see the radiation patterns for this model in Figure 3.8. Equation 3.35 is only relevant for the upper half-plane, as the reflector obstructs the other half.

We can once again apply the empirical factor as in the previous section:

$$U(\theta, \phi) = |E(\theta)2 \cos(k(0.5h) \cos \theta)|^2 + |C\sqrt{A} \cos(\phi)2 \cos(k(0.5h) \cos \theta)|^2 \quad (3.36)$$

This time, only the H-plane correction factor A is necessary, to which the ground plane factor is also applied. The directivity of this model is 8.8 dBi, while it is 9.5 dBi for the simulated one; patterns are shown in Figure 3.9.

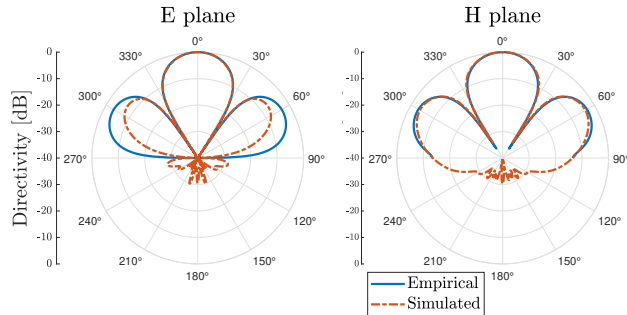


Figure 3.9: Uniform empirical model with a flat reflector and correction

3.4 Approximate model for the Franklin slot antenna

Let us now consider the uniform E-field distribution again, this time with an aperture shifted in x and y directions by a' and b' . This aperture of length a and b has its centre at a' and b' and the equation for E-field is:

$$\mathbf{E}_a = \begin{cases} \hat{\mathbf{y}}E_0, & \text{for } a' - \frac{a}{2} \leq x' \leq a' + \frac{a}{2} \text{ and } b' - \frac{b}{2} \leq y' \leq b' + \frac{b}{2} \\ \mathbf{0}, & \text{everywhere else.} \end{cases} \quad (3.37)$$

\mathbf{M}_s will be $\hat{\mathbf{y}}E_0$ once again, but for different aperture position. For this \mathbf{M}_s , we can write an equation for L_θ and L_ϕ as follows:

$$L_\theta = E_0 \cos \theta \cos \phi \left[\int_{b' - \frac{b}{2}}^{b' + \frac{b}{2}} \int_{a' - \frac{a}{2}}^{a' + \frac{a}{2}} e^{jk(x' \sin \theta \cos \phi + y' \sin \theta \sin \phi)} dx' dy' \right] \quad (3.38)$$

$$L_\phi = E_0 \sin \phi \left[\int_{b' - \frac{b}{2}}^{b' + \frac{b}{2}} \int_{a' - \frac{a}{2}}^{a' + \frac{a}{2}} e^{jk(x' \sin \theta \cos \phi + y' \sin \theta \sin \phi)} dx' dy' \right] \quad (3.39)$$

We can see that the only difference for L_θ and L_ϕ for this case are the altered integration bounds. We can still easily solve these integrals, and the change of bounds will only result in an additional exponential factor:

$$E_\theta^0 = C \left[\sin \phi \left(\frac{\sin X}{X} \right) \left(\frac{\sin Y}{Y} \right) e^{ja' \frac{2X}{a}} e^{jb' \frac{2Y}{b}} \right] \quad (3.40)$$

$$E_\phi^0 = C \left[\cos \theta \cos \phi \left(\frac{\sin X}{X} \right) \left(\frac{\sin Y}{Y} \right) e^{ja' \frac{2X}{a}} e^{jb' \frac{2Y}{b}} \right] \quad (3.41)$$

Equations (3.38) and (3.39) are the far-field E-fields for the shifted aperture. The additional exponential factors represent the aperture shifts in the x and y directions by a' and b' . We can use this model to find the radiation patterns for Franklin slot antennas, which we examine in further chapters.

These antennas have the aperture shape of a Franklin antenna from section 2.4. We can get a model for the Franklin antenna as a collinear array of half-wave dipoles representing Franklin antenna radiating elements. Instead of approaching this problem as an antenna array problem, we can obtain the total E-field caused by multiple collinear slots as a superposition of their E-fields obtained from equations (3.38) and (3.39). As it turns out, collinear slot stacking only affects the H-plane's radiation pattern, while the E-plane remains the same as for a single slot. We will thus consider the E-field from Equation 3.33 as the E-plane E-field and only use the superposition for the H-plane E-field. For the H-plane, we will use a variation of Equation 3.33 with the added exponential factor for shifts in the x direction. We will then sum up the individual E-fields shifted by a_n to obtain the total E-field.

$$U(\theta, \phi = 0^\circ) = \left| \sum_{n=1}^N C \cos \theta \left(\frac{\sin X_\theta}{X_\theta} \right) e^{ja'_n \frac{2X_\theta}{a}} \right|^2 \quad (3.42)$$

$$U(\theta, \phi = 90^\circ) = \left| C \cos \theta \left(\frac{\sin X_\theta}{X_\theta} \right) \right|^2 \quad (3.43)$$

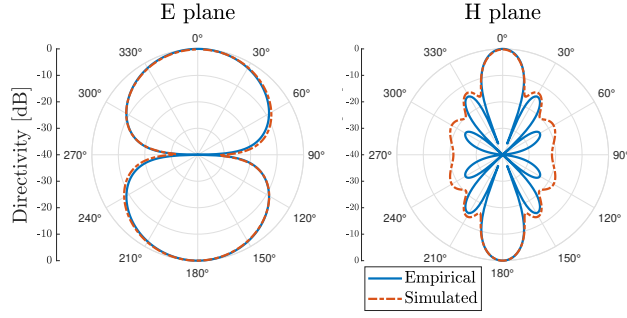


Figure 3.10: Simple model for a five-element Franklin slot antenna

The equations (3.42) and (3.43) represent the radiation intensity for our model of the Franklin slot antenna only in the E and H planes; we cannot thus calculate the directivity for this model. If we wished to do so, we would need to stitch these two patterns together, resulting in a 3D characteristic.

In Figure 3.10, we compare this model to a simulated 10 GHz Franklin slot model with a discrete port and with the dimensions of the second antenna in section 5.3. As we can see, the radiation pattern in the E-plane matches the simulation well, as does the main lobe in the H-plane. The direction for the respective sidelobes in the H-plane also matches well; however, the sidelobe region's directivity levels are lower than the simulated results. We can once again apply the correction for the truncated ground plane, as we did in the previous sections 3.2 and 3.3:

$$U(\theta, \phi = 0^\circ) = \left| \sum_{n=1}^N C \cos \theta \left(\frac{\sin X_\theta}{X_\theta} \right) e^{ja'_n \frac{2X_\theta}{a}} \right|^2 + |C\sqrt{A}|^2 \quad (3.44)$$

$$U(\theta, \phi = 90^\circ) = \left| C \cos \theta \left(\frac{\sin X_\theta}{X_\theta} \right) \right|^2 + |C\sqrt{B}|^2 \quad (3.45)$$

In these equations, the corrective factors no longer require the sine and cosine factors, as we only calculate the radiation patterns in the E and H planes. We can see these radiation patterns with the correction in Figure 3.11. As we can see, the E-plane pattern is almost spot-on, while the H-plane pattern also closely resembles the simulated one. Note that this pattern is only valid for a frequency of 10 GHz, as other ones will have altered E-field distributions.

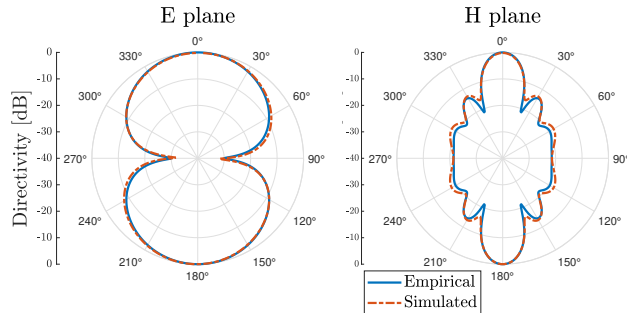


Figure 3.11: Model for a five-element Franklin slot antenna with corrections

Chapter 4

Franklin slot antenna as a thin PEC sheet

4.1 Three-element Franklin slot antenna

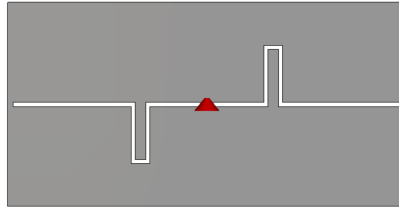


Figure 4.1: Three-element Franklin slot antenna

We can obtain a Franklin slot antenna by combining the principles of a slot and a Franklin antenna. Such an antenna has a cutout of the shape of a Franklin antenna of width w_{slot} , wavelength λ and gap w_{gap} in a rectangular ground plane of width w_{gnd} and length l_{gnd} . We modelled this antenna in CST with phasing elements in opposite directions, as shown in Figure 4.1. We simulated this antenna for dimensions of $w_{\text{slot}} = 0.7$ mm, $w_{\text{gap}} = 3$ mm, $w_{\text{gnd}} = 80$ mm and $l_{\text{gnd}} = 220$ mm operating at 2.5 GHz with $\lambda = 120$ mm, as can be seen in Figure 4.6 and has a bandwidth of 14.3 % and a directivity of 8.85 dBi. We also simulated this antenna with different values for these dimensions. The results are shown in Figures 4.2 to 4.5.

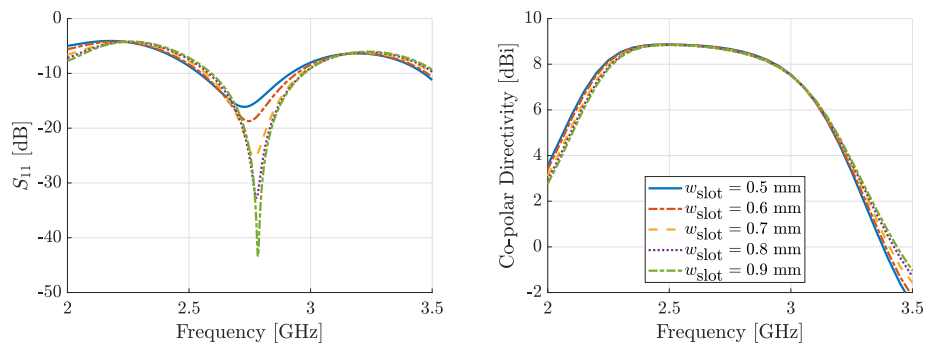


Figure 4.2: Three-element Franklin slot performance for different w_{slot}

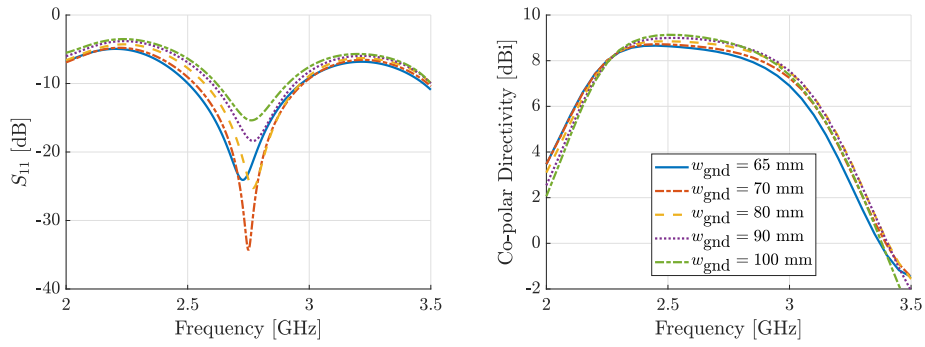


Figure 4.3: Three-element Franklin slot performance for different w_{gnd}

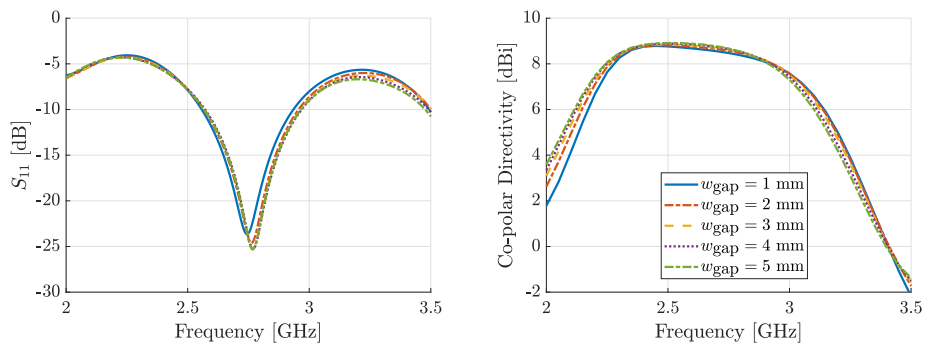


Figure 4.4: Three-element Franklin slot performance for different w_{gap}

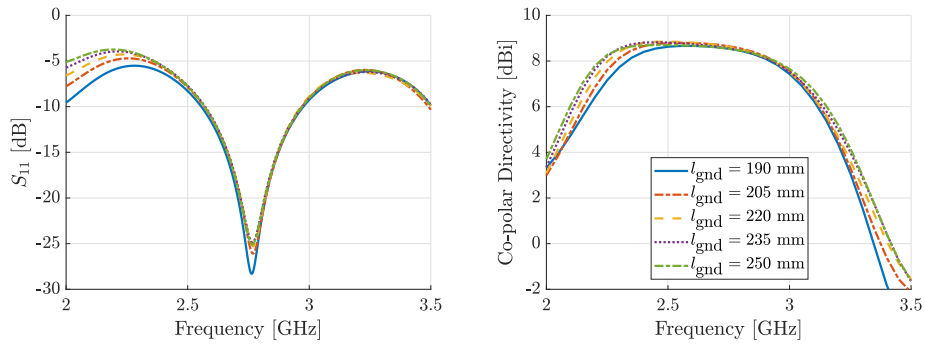


Figure 4.5: Three-element Franklin slot performance for different l_{gnd}

We can see that out of these parameters, the width of the ground plane w_{gnd} and the width of the slot w_{slot} are to be chosen with significant consideration as they affect the input matching. Antenna with smaller w_{gnd} will have better bandwidth but a smaller directivity. Parameters w_{gap} and l_{gnd} can be chosen more freely, as they do not affect the antenna behaviour as much.

In Figure 4.6, we can see that the bandwidth of this antenna is limited by its impedance match, as the radiation bandwidth is relatively wide. The antenna has a wide beamwidth in the E-plane and a narrower beamwidth in the H-plane. We can also see that this antenna has a cross-polarisation ratio of 17.4 dB in the main radiating directions.

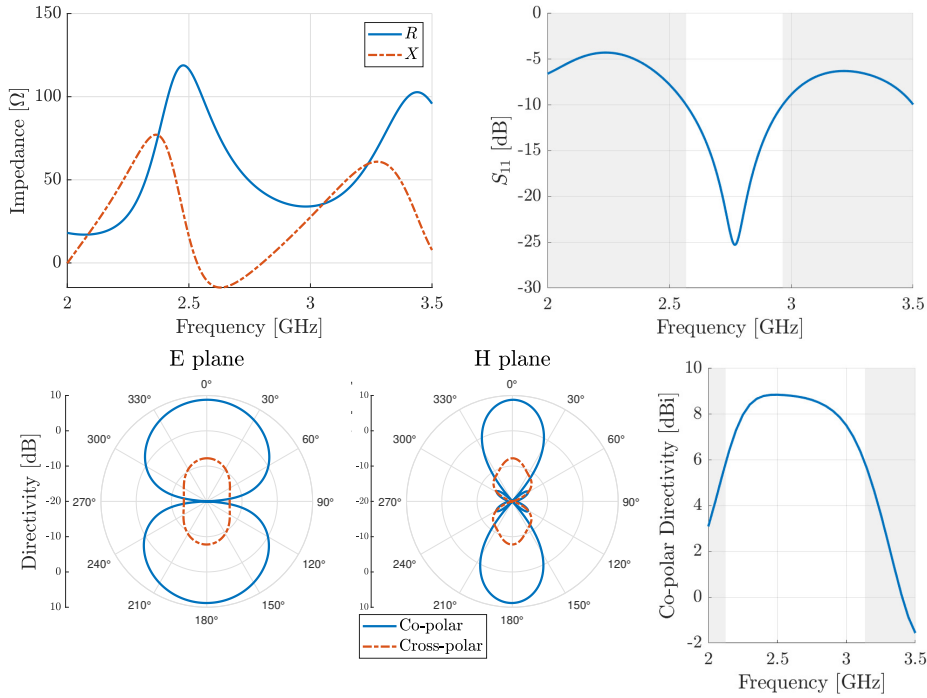


Figure 4.6: Parameters of simulated three-element Franklin slot antenna

4.2 Five-element Franklin slot antenna

We can add two more radiating elements to the Franklin slot antenna; we now have more options on the phase element orientation to maintain diagonal symmetry, as shown in Figure 4.7. Option A has the phasing elements on each side facing the same direction, while Option B has the phasing elements facing the opposite direction. Option C uses symmetrical O-shaped phasing elements facing both directions and is fully symmetrical. We modelled and simulated these antennas in CST with dimensions of $w_{\text{slot}} = 0.6$ mm, $w_{\text{gap}} = 3$ mm, $w_{\text{gnd}} = 80$ mm, $l_{\text{gnd}} = 350$ mm and $\lambda = 120$ mm. We can see simulated results for these antennas in Figure 4.8.

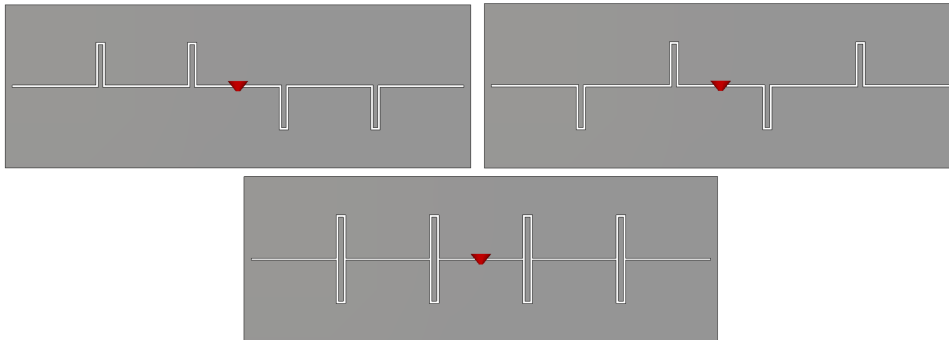


Figure 4.7: Variants of five-element Franklin slot antennas

4. Franklin slot antenna as a thin PEC sheet

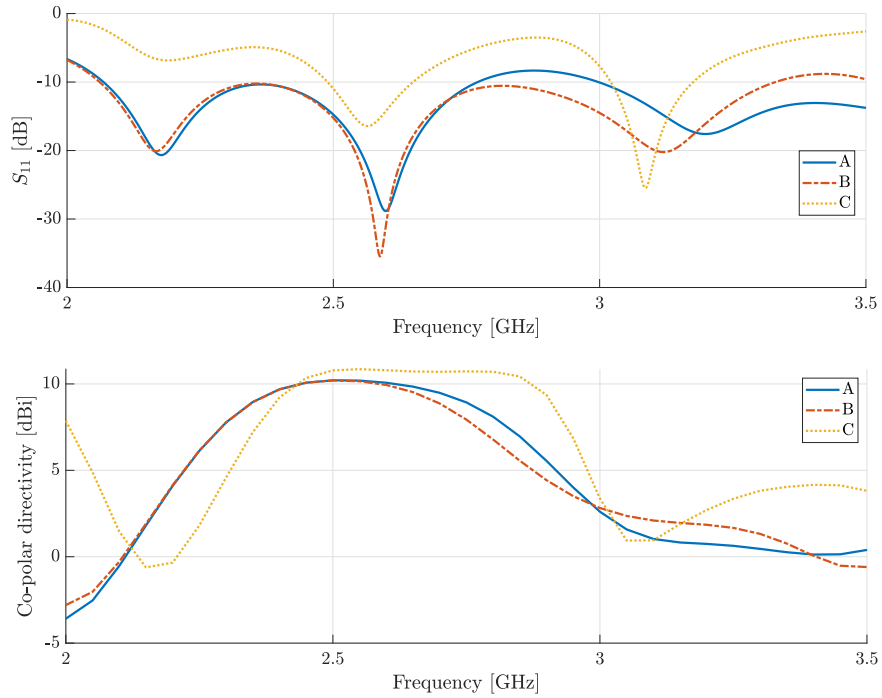


Figure 4.8: Performance of the three phasing element configurations

We can see that Option C has the best radiation performance; however, it has a poor impedance match compared to the other options, and it is also more complicated as it comprises five separate pieces instead of one. Option B achieves the highest matching bandwidth, but most of the matched region is unnecessary as the radiation bandwidth now limits the antenna bandwidth. Option A has a slightly wider radiation bandwidth; we will use it predominantly in this thesis, even though it has a smaller matching bandwidth than option B. We can see the radiation pattern for Option A in Figure 4.9. The beamwidth in the E-plane remains the same as in the three-element antenna, and the beamwidth in the H-plane gets narrower for the five-element configuration. We can also see increased cross-polar directivity for the five-element antenna, with the x-pol ratio being 11.9 dB. Option A

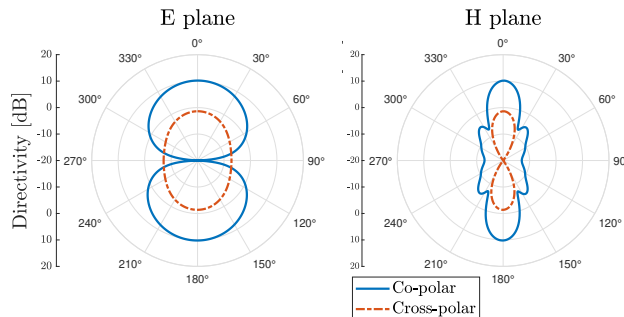


Figure 4.9: Radiation pattern for Option A five-element Franklin slot antenna



Figure 4.10: Five-element antenna with phasing elements facing one direction

achieves a radiation bandwidth of 21.8 % and a matching bandwidth of 29 %.

The x-pol ratio for Option A in the radiating direction is lower than we would desire. Option C offers the best polarisation cleanliness but achieves poor matching. The vertical symmetry of Option C is the reason for the polarisation cleanliness. We can achieve vertical symmetry by making the phasing elements face a single direction, as shown in Figure 4.10. Such an antenna has an extra parameter due to the loss of diagonal symmetry as we now need to describe the offset of the slot centre from the bottom of the ground plane w_{offset} . We simulated this structure in CST with dimensions of $w_{\text{slot}} = 0.6$ mm, $w_{\text{gap}} = 3$ mm, $w_{\text{gnd}} = 52$ mm, $l_{\text{gnd}} = 325$ mm, $w_{\text{offset}} = 17$ mm and $\lambda = 120$ mm. We can see the results in Figure 4.11.

Cross-polarisation is negligible in the E-plane and in the direction of the main lobes for this structure due to the vertical symmetry. However, cross-polarisation is still significant for the other directions, as seen in the H-plane in Figure 4.11, which also shows the maximum cross-polar directivity in the H-plane based on the frequency. The matching of this structure is similar to Option B, having a wide matching bandwidth of 47.9 % but a narrower radiation bandwidth of 20.3 %. Directivity is slightly smaller, being 9.7 dBi.

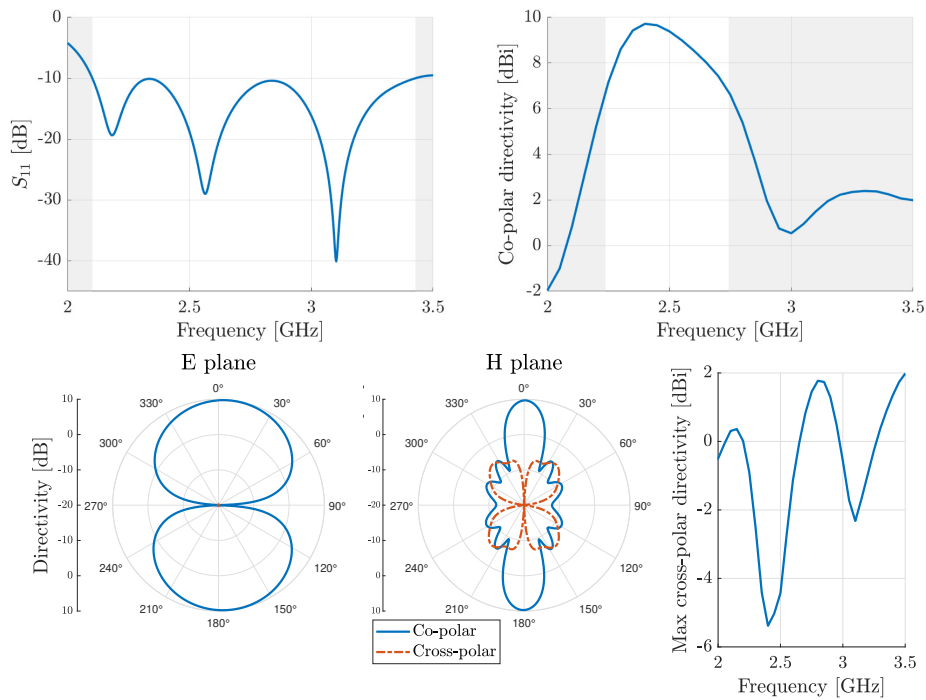


Figure 4.11: Performance of antenna with phasing elements in one direction

4.3 Franklin slot antennas with more elements

Adding more elements improves directivity; however, the increment of the directivity decreases. In Figure 4.12, we can see the simulated S parameters and directivity for both polarisations for antennas with different amounts of radiating elements. We can see that antennas with more elements achieve better matching and broader matching bandwidth; however, their radiation bandwidth gets narrower than for those with fewer radiating elements. The cross-polarisation level also increases with increasing number of elements.

The antenna with five radiating elements performs best as it has a much better matching and higher directivity than the three-element antenna. It also has a broader radiation bandwidth, lower cross-polarisation, and is more compact than the seven-element one. We will thus only consider the five-element antenna further on in the thesis.

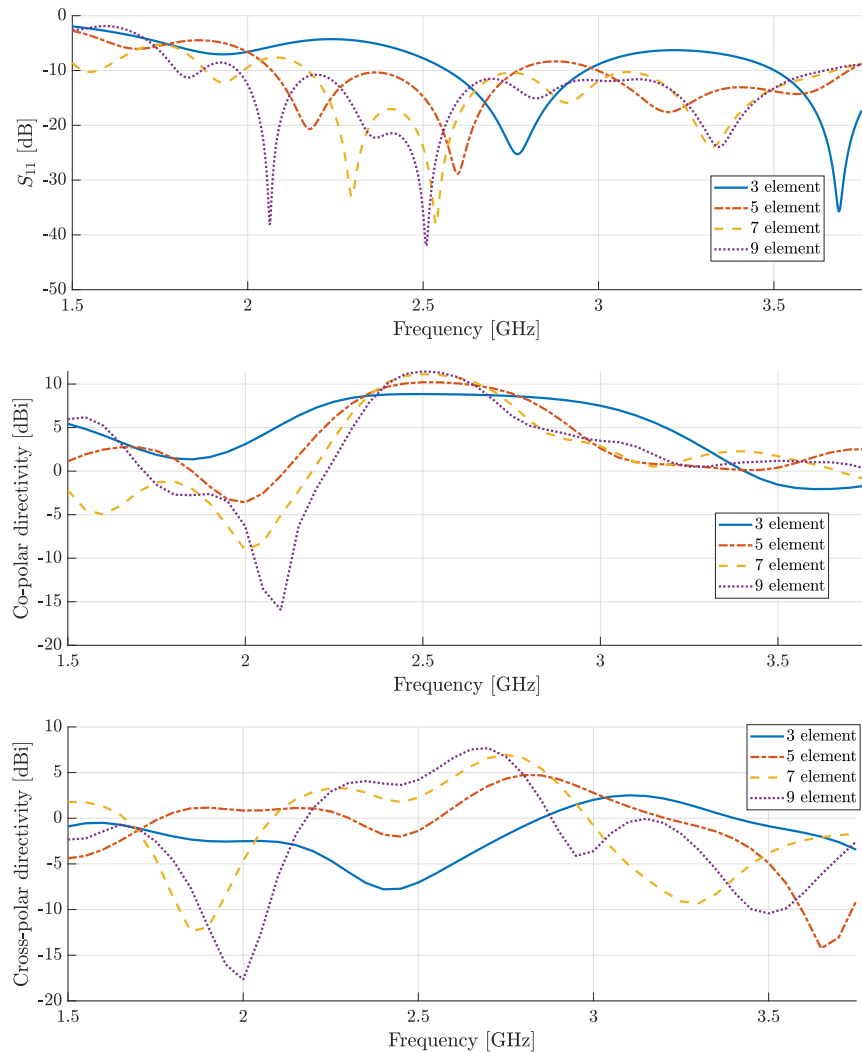


Figure 4.12: Parameters of antennas with N radiating elements

Chapter 5

Franklin slot antenna on FR4 substrate

5.1 Effects of FR4 substrate

In this chapter, we will model the Franklin slot antenna as a conductive layer of copper of height h_{Cu} placed on top of an FR4 substrate of height h_{FR4} and relative permittivity ϵ_r . Figure 5.1 compares the previous chapter's five-element PEC Franklin slot antenna to the new equivalents. We simulated these antennas in CST with dimensions of $w_{\text{gap}} = 3$ mm, $w_{\text{gnd}} = 80$ mm, $l_{\text{gnd}} = 350$ mm and $\lambda = 120$ mm. The antenna from a thin PEC sheet had $w_{\text{slot}} = 0.6$ mm, whilst the new antennas had $w_{\text{slot}} = 1$ mm. The new antennas also had $h_{\text{Cu}} = 35$ μm , $h_{\text{FR4}} = 0.6$ mm and $\epsilon_r = 4.3$. We chose pure copper and lossy FR4 as the material presets for these models from the CST material library. One of these new antennas was modelled with

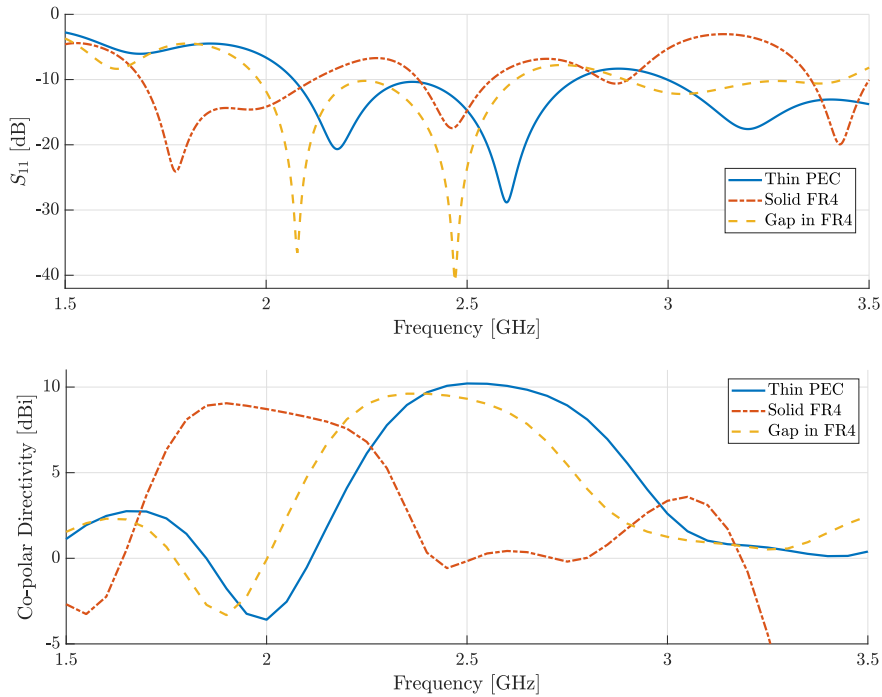


Figure 5.1: Comparison between PEC and FR4 Franklin slot antenna models

solid FR4 substrate, whilst the other one had the same cutout in the FR4 as in the copper layer. As we can see in Figure 5.1, the model with a solid FR4 substrate lowers the operating frequency by increasing the guided wavelength λ_g due to higher ϵ_r near the slot. FR4 near the slot also hurts the antenna's directivity. Introducing a cutout in the FR4 substrate can negate some of the FR4 influence and make it more comparable to the PEC model.

There is still some difference between the performance of a Franklin slot antenna as a thin PEC sheet and as a copper layer on an FR4 substrate with a cutout in the substrate. Fringing fields of the antenna on the FR4 substrate are partially affected by the substrate's permittivity and cause this difference. We can negate this effect by metalising the slot cutout's inner surface, creating a more uniform field distribution in the slot and significantly reducing the substrate's influence on the fringing fields. Figure 5.2 shows this improvement: the antenna's performance with the metalised slot is comparable to the thin PEC sheet antenna from Figure 5.1. Metallisation of the inside of the slot is also beneficial from the PCB manufacturing perspective as the manufacturers can create a narrower slot width w_{slot} for these slots.

Figure 5.2 also shows the performance of a Franklin slot antenna with copper metallisation on both faces and inside the slot cutout. Such configuration offers slightly improved directivity but also marginally worse matching. Both options seem viable, but in this thesis, we will proceed with a single metalised face and inner slot surface because of the slightly better matching resembling the PEC variant matching. The operating region's S_{11} peak is now higher than the required -10 dB for these variations. This peak will be reduced in section 5.2 by replacing the discrete port with a coaxial feed.

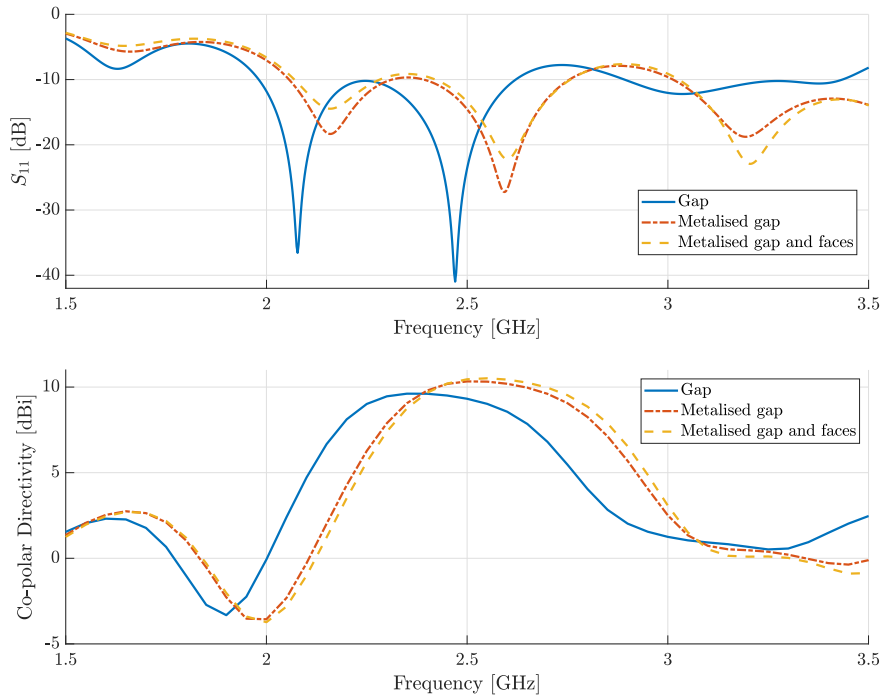


Figure 5.2: Performance of antennas with additional metalisation

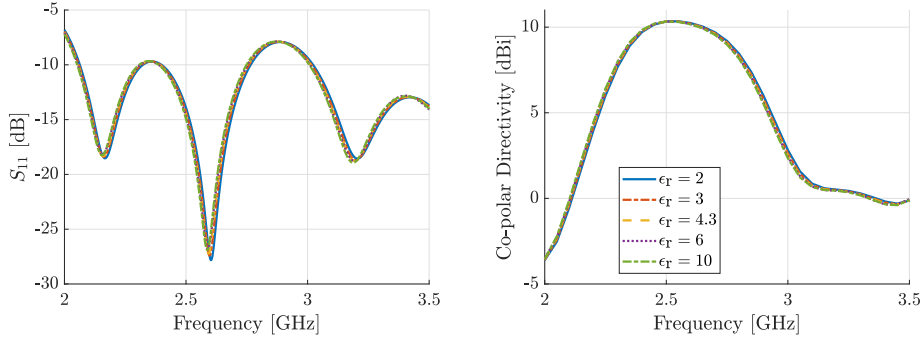


Figure 5.3: Franklin slot antenna performance for different substrate ϵ_r

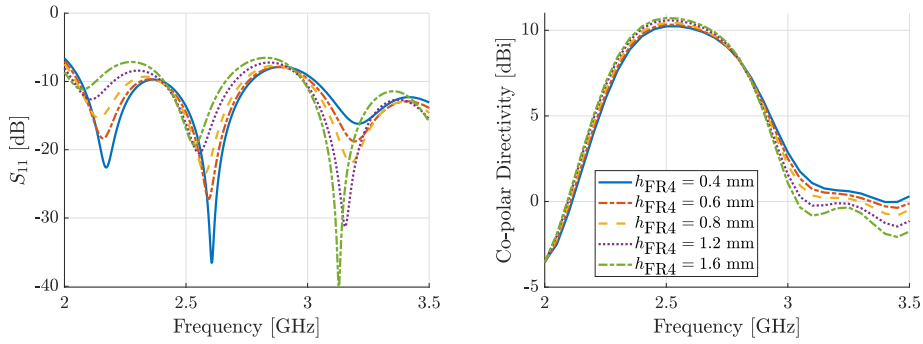


Figure 5.4: Franklin slot antenna performance for different h_{FR4}

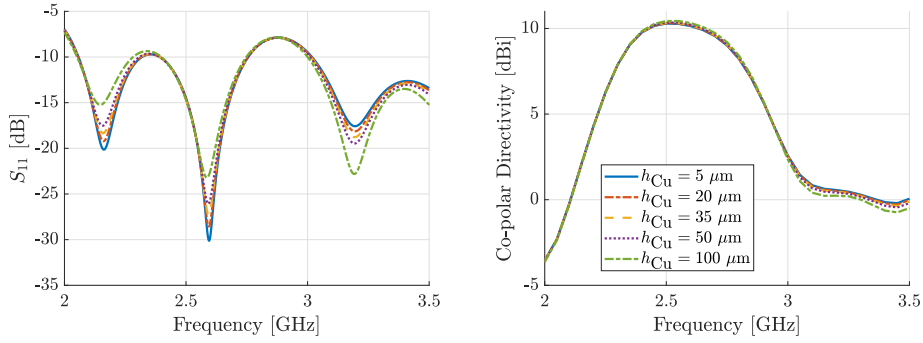


Figure 5.5: Franklin slot antenna performance for different h_{Cu}

Figures 5.3, 5.4 and 5.5 show the antenna performance for different values of substrate relative permittivity ϵ_r , substrate height h_{FR4} offered by the PCB manufacturer and metallisation height h_{Cu} . We can see that the antenna's performance is not affected by different values of ϵ_r ; this is beneficial since the FR4 substrate does not offer good dimensional permittivity stability and the manufacturer does not guarantee the exact value of ϵ_r . We can also see that the substrate height h_{FR4} should be chosen with consideration as greater values of h_{FR4} tend to have poor matching performance but achieve higher directivity. Lastly, we can see that the height of the metallisation layer h_{Cu} has only minimal impact on the antenna performance.

5.2 Model with coaxial feed

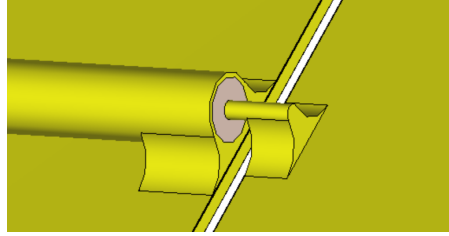


Figure 5.6: Coaxial feed modelled for the antenna

Until now, we have been simulating the Franklin slot antennas with a discrete port. We will now model the antennas with a coaxial feed instead. Coaxial cable is characterised by an inner radius r_a , outer radius r_b , exterior radius r_c and a relative dielectric permittivity ϵ_r . For a coaxial cable to have a certain characteristic impedance Z_0 , we should use a coaxial cable with the outer radius obtained from the following equation:

$$r_b = r_a e^{\frac{Z_0 \sqrt{\epsilon_r}}{60}} \quad (5.1)$$

We can see the connection between the coaxial cable and the centre radiating slot in Figure 5.6. The modelled connection mimics physical soldered contact and should only be near the slot for best performance. We simulated the Franklin slot antenna with the metalised slot from the previous section with coaxial feeds of different values of r_a . The coaxial cable used PTFE dielectric from the CST material library with the $\epsilon_r = 2.1$, its r_b was calculated for a characteristic impedance of 50Ω and its $r_c = r_b + 0.5r_a$. We can see the simulated results in Figure 5.7. As we can see, the coaxial cable size impacts the antenna performance even though the characteristic impedance remains the same. The antenna model with a thin coaxial cable achieves worse matching than even the discrete port variant; however, the model with a thicker coaxial cable sees an improvement in the matching that effectively decreases the S_{11} peaks. Coaxial cables with the r_a greater than half the slot width of the antenna should be used for good performance.

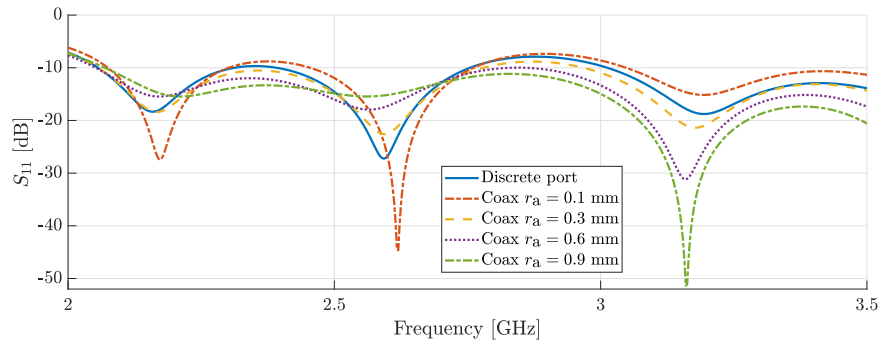


Figure 5.7: Franklin slot antenna S parameters for different coaxial r_a

5.3 Models for realised antennas

2.5 GHz Franklin slot antenna

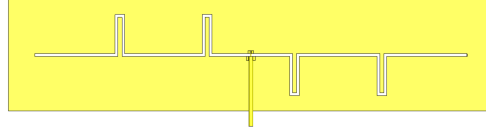


Figure 5.8: Realised 2.5 GHz Franklin slot antenna

We can see the model for the 2.5 GHz realised antenna in Figure 5.8. Dimensions for this antenna are $w_{\text{gap}} = 3$ mm, $w_{\text{gnd}} = 80$ mm, $l_{\text{gnd}} = 350$ mm, $w_{\text{slot}} = 1.1$ mm, $\lambda = 120$ mm, $h_{\text{Cu}} = 35$ μm and $h_{\text{FR4}} = 0.6$ mm with the coaxial cable $r_a = 0.4$ mm. We can see the simulated characteristics of this antenna in Figure 5.9. This antenna has a matching bandwidth of 30.7 % and a radiating bandwidth of 21.8 %—the bandwidth where these two overlap is 20.2 %, with the centre frequency being 2.55 GHz. The co-polar directivity of this antenna in the main direction at the centre frequency is 10.3 dBi, and the x-pol ratio is 10.6 dB. In the E-plane, this antenna has a wide main lobe with an HPBW of 68.6°; in the H-plane, the main lobe is much narrower with an HPBW of 20.7°. The direction of the main lobe is shifted by 1 degree in the E-plane, and the radiation pattern is relatively uniform. Sidelobes are only present in the H-plane with the SLL of -16 dB.

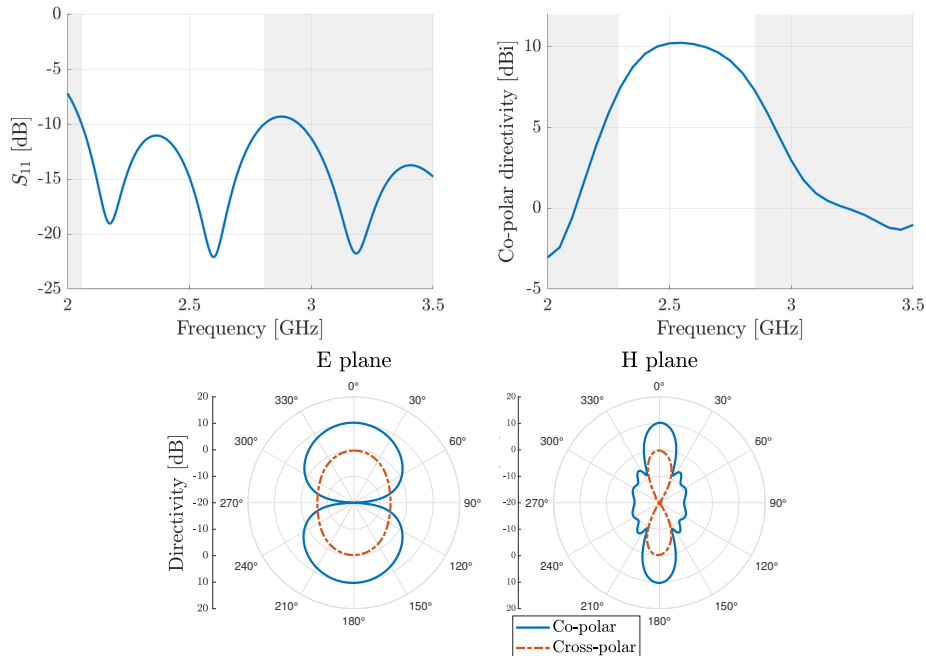


Figure 5.9: Performance of the realised 2.5 GHz Franklin slot antenna

10 GHz Franklin slot antenna

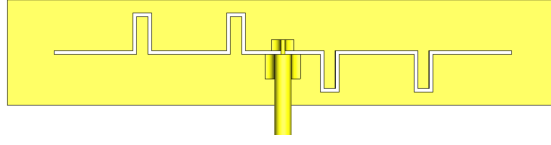


Figure 5.10: Realised 10 GHz Franklin slot antenna

We can see the model for the 10 GHz realised antenna in Figure 5.10. We modelled this antenna using the same model as the 2.5 GHz antenna with the following dimensions $w_{\text{gap}} = 2$ mm, $w_{\text{gnd}} = 19$ mm, $l_{\text{gnd}} = 100$ mm, $w_{\text{slot}} = 0.7$ mm, $\lambda = 30$ mm, $h_{\text{Cu}} = 35$ μm and $h_{\text{FR4}} = 0.6$ mm with the coaxial cable $r_a = 0.4$ mm. Figure 5.11 shows the simulated results for this antenna. This antenna has a slightly improved matching bandwidth of 31.4 % and an improved radiating bandwidth of 23.5 %—the bandwidth where these two overlap is 22.1 %, which is slightly higher than for the 2.5 GHz antenna, with the centre frequency being 10.18 GHz. The co-polar directivity of this antenna in the main direction at the centre frequency is 10.7 dBi, which is again better, and the cross-polarisation ratio is 11.1 dB. In the E-plane, this antenna has a wide main lobe with an HPBW of 64.7°; in the H-plane, the main lobe is much narrower with an HPBW of 18.8°. The direction of the main lobe is shifted by 4 degrees in the E-plane, and the radiation pattern is not uniform due to the coaxial cable presence. Sidelobes are only present in the H-plane with the SLL of -15.4 dB.

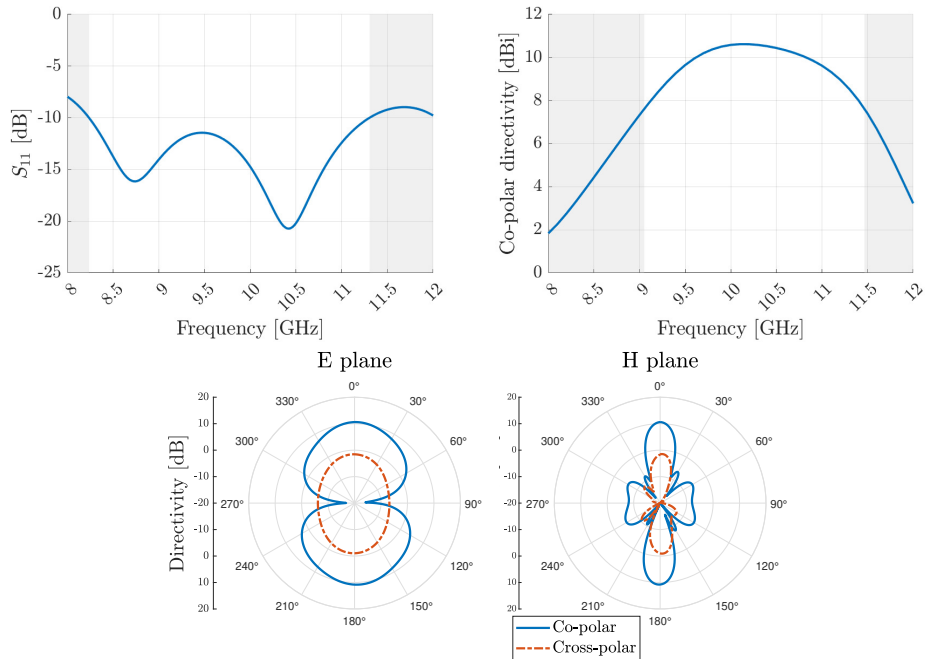


Figure 5.11: Performance of the realised 10 GHz Franklin slot antenna

10 GHz Franklin antenna slot with phasing elements on one side

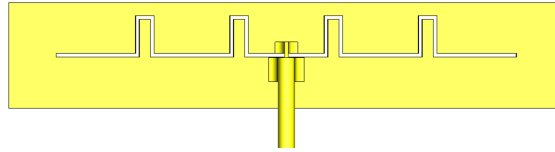


Figure 5.12: Realised 10 GHz antenna with phasing elements in one direction

We have also modelled and realised a 10 GHz antenna version with all phasing elements on one side; we can see this model in 5.12. We modelled this antenna with the exact dimensions of the previous 10 GHz antenna and retained the position of the radiating elements for this antenna. We can see the results for this antenna in Figure 5.12. This antenna has a very high matching bandwidth of 56.7 % but a slightly smaller radiating bandwidth of 20.8 % compared to the previous 10 GHz antenna. The bandwidth of this antenna is purely limited by its radiating bandwidth, with the centre frequency being 10.21 GHz. The co-polar directivity of this antenna in the main direction at the centre frequency is 10.7 dBi, and the cross-polarisation is negligible. In the E-plane, this antenna has a wide main lobe with an HPBW of 63.3°; in the H-plane, the main lobe is much narrower with an HPBW of 18.1°. The direction of the main lobe is shifted by 10 degrees in the E-plane, and the radiation pattern is even less uniform. Sidelobes are only present in the H-plane with the SLL of -16.1 dB.

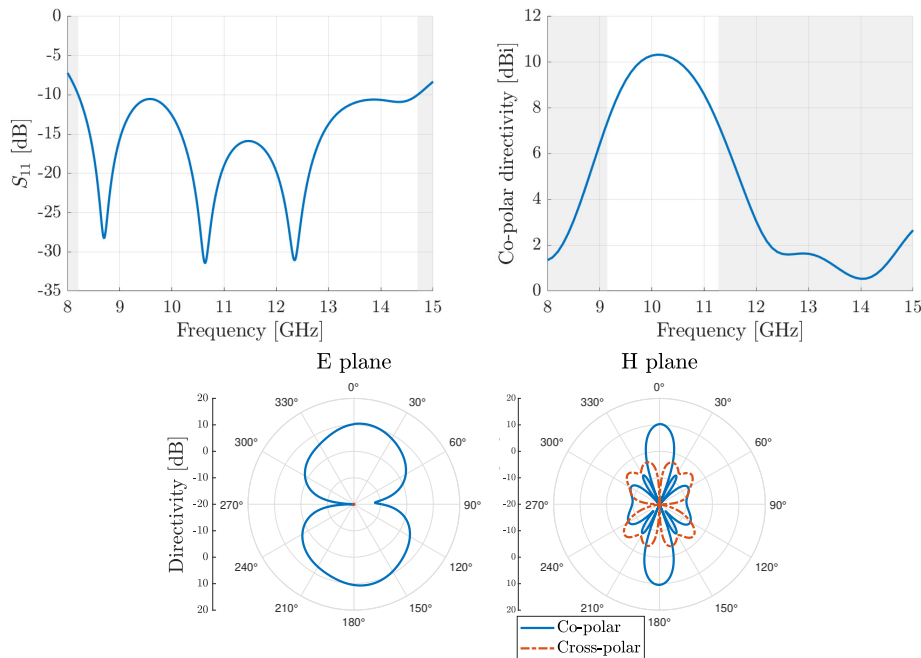


Figure 5.13: Performance of the realised 10 GHz antenna with phasing elements in one direction

First iteration of 10 GHz Franklin slot antenna with different slot geometry

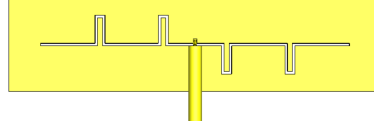


Figure 5.14: Realised first iteration of the 10 GHz antenna

The first realised iteration of the 10 GHz antenna, which we can see in Figure 5.14, was made with a slightly different slot geometry. Each slot segment's length was affected by the fraction of λ and the slot width w_{slot} . Respective $\frac{\lambda}{2}$ and $\frac{\lambda}{4}$ thus represent the line in the middle of the slot. We modelled this antenna with dimensions $w_{\text{gap}} = 1.3$ mm, $w_{\text{gnd}} = 25$ mm, $l_{\text{gnd}} = 100$ mm, $w_{\text{slot}} = 0.7$ mm, $\lambda = 30$ mm, $h_{\text{Cu}} = 35$ μm and $h_{\text{FR4}} = 0.8$ mm with the coaxial cable $r_a = 0.4$ mm. Figure 5.15 shows the simulated results for this antenna. The matching bandwidth for this antenna is much lower than the other ones, being 9.25 %, with the centre frequency being 9.87 GHz. The co-polar directivity of this antenna in the main direction at the centre frequency is 10.7 dBi, and the cross-polarisation ratio of 10.9 dB. In the E-plane, this antenna has a wide main lobe with an HPBW of 65.8°; in the H-plane, the main lobe is much narrower with an HPBW of 19.2°. The direction of the main lobe is shifted by 1 degree in the E-plane, and the radiation pattern is not uniform due to the coaxial cable presence.

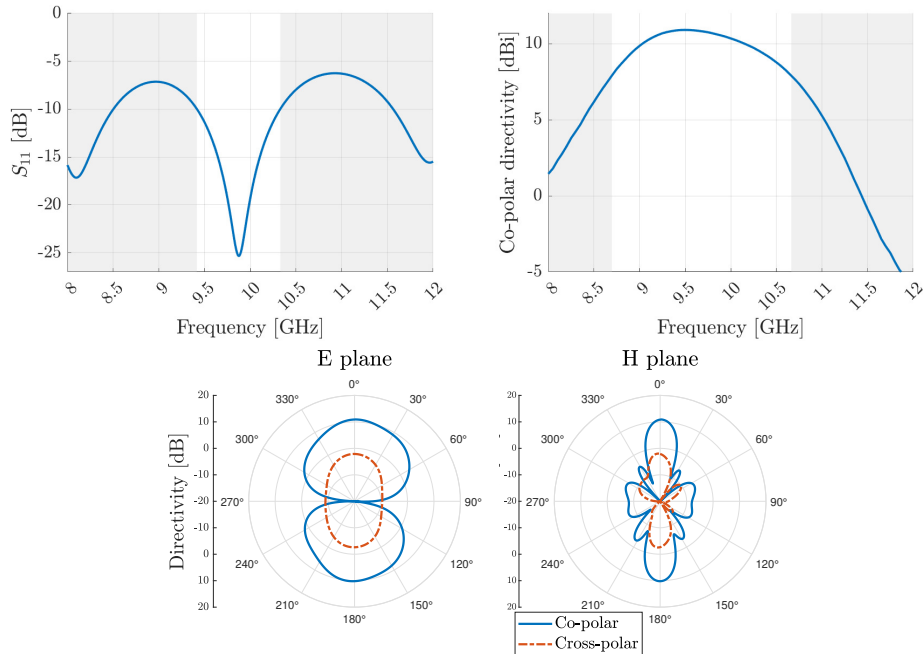


Figure 5.15: Performance of the realised 10 GHz first iteration antenna

5.4 Reflectors for Franklin slot antennas

Flat reflector

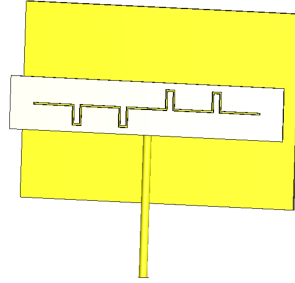


Figure 5.16: 10 GHz Franklin slot antenna with a flat reflector

We can add a flat reflector to the Franklin slot antenna to make it unidirectional and increase its directivity. We can see such a configuration in Figure 5.16. The reflector was modelled as a rectangular copper layer of width $w_{\text{Cu}} = 35 \mu\text{m}$ on an FR4 substrate of width w_{ref} and length l_{ref} spaced by distance d_{ref} from the antenna. For best performance, the metallised face of the antenna should face the reflector. We simulated this model with the first and second iterations of the 10 GHz Franklin slot antenna. The spacing distance d_{ref} was 18 mm for both antennas. The first iteration was realised and modelled with a reflector of size $w_{\text{ref}} = 127 \text{ mm}$ and $l_{\text{ref}} = 230 \text{ mm}$ as this was the size of an available copper clad board. The second iteration was modelled with a reflector of $w_{\text{ref}} = 58 \text{ mm}$ and $l_{\text{ref}} = 100 \text{ mm}$; however, we did not realise it as the version with the V-shaped reflector performs better.

In Figures 5.17 and 5.18, we can see the simulated results of the second iteration antenna with the flat reflector for different values of w_{ref} and d_{ref} . As we can see, we should pick these dimensions carefully as they affect both the matching and directivity. The antenna performance is significantly affected by changes in the spacing distance. The reflector length l_{ref} should be at least the same length as the length of the Franklin slot antenna l_{gnd} . Any additional increase of l_{ref} does not affect the antenna performance much.

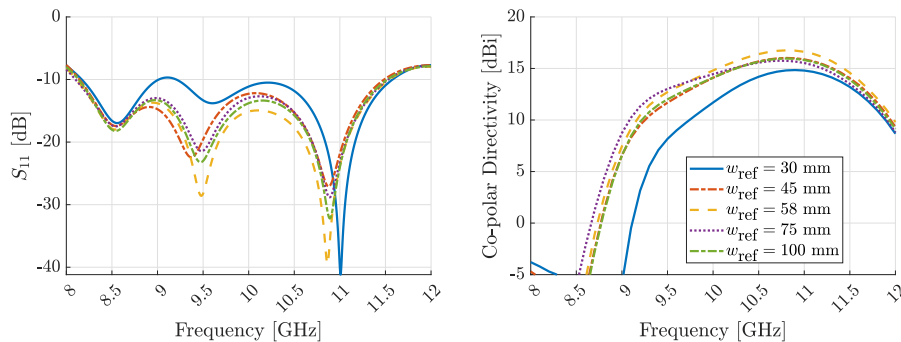


Figure 5.17: Flat reflector antenna performance for different w_{ref}

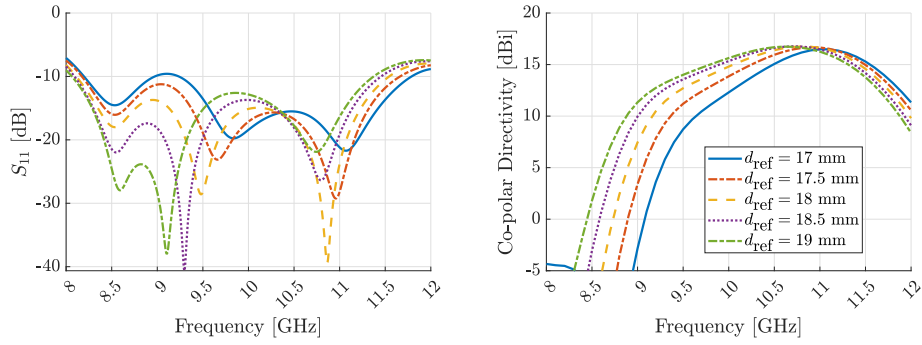


Figure 5.18: Flat reflector antenna performance for different d_{ref}

We can see the simulated results for these two antenna iterations in Figure 5.19. Adding the flat reflector improves the matching of these antennas and increases their bandwidth. The radiation bandwidth predominantly limits the bandwidth of these antennas, which is 9.5 % and 16.9 % for the first and second iterations. The addition of the reflector also increases the centre frequency to 10.1 GHz and 10.6 GHz for these antennas, respectively. We can see that the antennas are now unidirectional, with the co-polar directivity increasing to 16.3 dBi and 16.8 dBi and the cross-polarisation ratio being 12.8 dB and 11.8 dB. The main lobe in the E-plane is now much narrower, being 28.5° and 28.2° for the two versions. The main lobe in the H-plane is of similar width as without the reflector, being 17.3° and 17.4°. The direction of the main lobe is shifted by 1 degree in the E-plane for both versions.

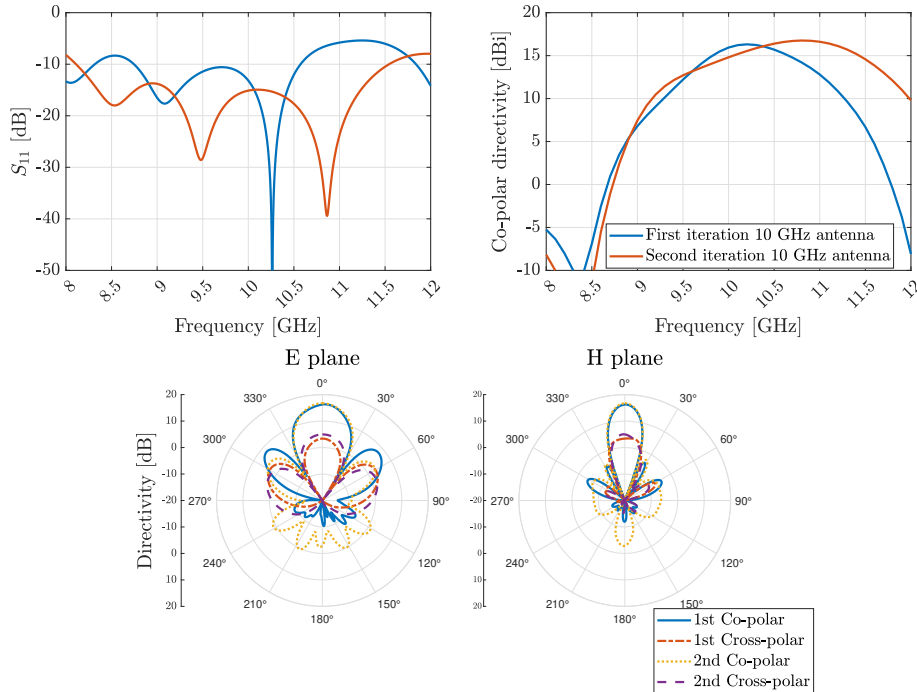


Figure 5.19: Performance of 10 GHz antennas with the flat reflector

V-shaped reflector

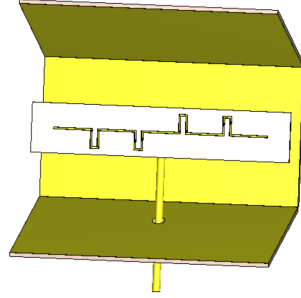


Figure 5.20: 10 GHz Franklin slot antenna with a V-shaped reflector

As the frequency of the Franklin slot antenna with the flat reflector decreases, the directivity of the main beam will decrease as well; however, the directivity of the sidelobes in the E-plane will start to increase. Two additional sub-reflectors can direct these sidelobes toward the main lobe. Figure 5.20 shows such a model with a V-shaped reflector composed of a flat reflector with two additional slanted subreflectors by an angle θ_{ref} . One of these has an additional hole cutout for the coaxial cable. These subreflectors have the same length l_{ref} and width w_{ref} as the flat reflector for simplicity. We simulated and realised this model with the second iteration and the second iteration with one-sided phasing elements of the Franklin slot antenna with the reflector dimensions $l_{\text{ref}} = 100$ mm and $w_{\text{ref}} = 53$ mm with the angle of the slanted subreflectors $\theta_{\text{ref}} = 23^\circ$ and $d_{\text{ref}} = 18$ mm.

In Figures 5.17 and 5.18, we can see the simulated results of the second iteration antenna with the V-shaped reflector for different values of θ_{ref} and w_{ref} . These two dimensions, together with the flat reflector spacing d_{ref} , should be chosen carefully for the best antenna performance. The same d_{ref} should be used as with the flat reflector antenna. The flat reflector's width and the subreflectors' width could be treated as two separate values for slightly better performance. We can see, that w_{ref} affects matching and directivity more than θ_{ref} . Once again, the length of the reflectors l_{ref} should be at least the same as the length of the Franklin slot antenna l_{slot} .

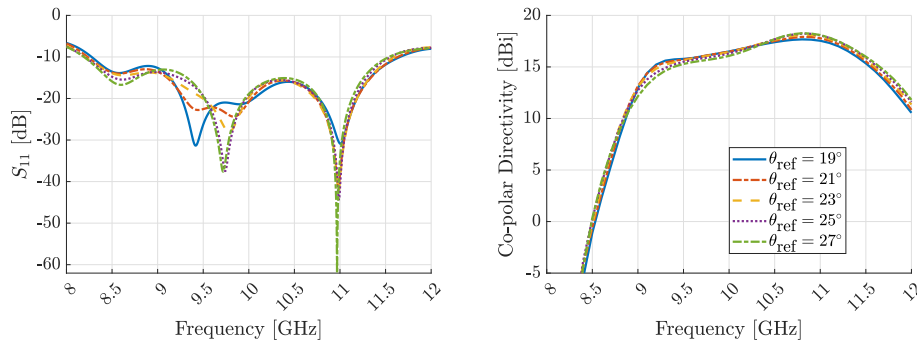


Figure 5.21: V-shaped reflector antenna performance for different θ_{ref}

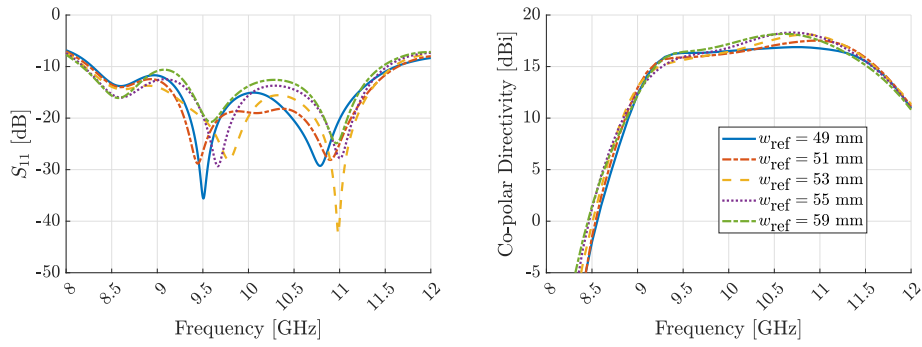


Figure 5.22: Franklin slot antenna performance for different w_{ref}

Figure 5.23 shows the simulated result for the two versions of the antennas with the V-shaped reflectors. The V-shaped reflector variant performs similarly to the flat reflector variant in terms of input characteristics, but the radiation bandwidth of the V-shaped reflector variant is improved. The antenna bandwidth is now fully limited by the radiation bandwidth and is 22.1 % and 22.7 %, and the centre frequency is now 10.4 GHz and 10.3 GHz for these two antenna variations, respectively. The co-polar directivity for this reflector variation increases to 18.1 dBi and 17.9 dBi. We can see that the sidelobes in the E-plane have been directed to the main lobe direction, leading to an HPBW of 20.9° for both versions. Sidelobes now appear in the H-plane, where the HPBW is 18.5° and 18.7°, respectively. The antenna version with one-sided phasing elements performs better in terms of cross-polarisation.

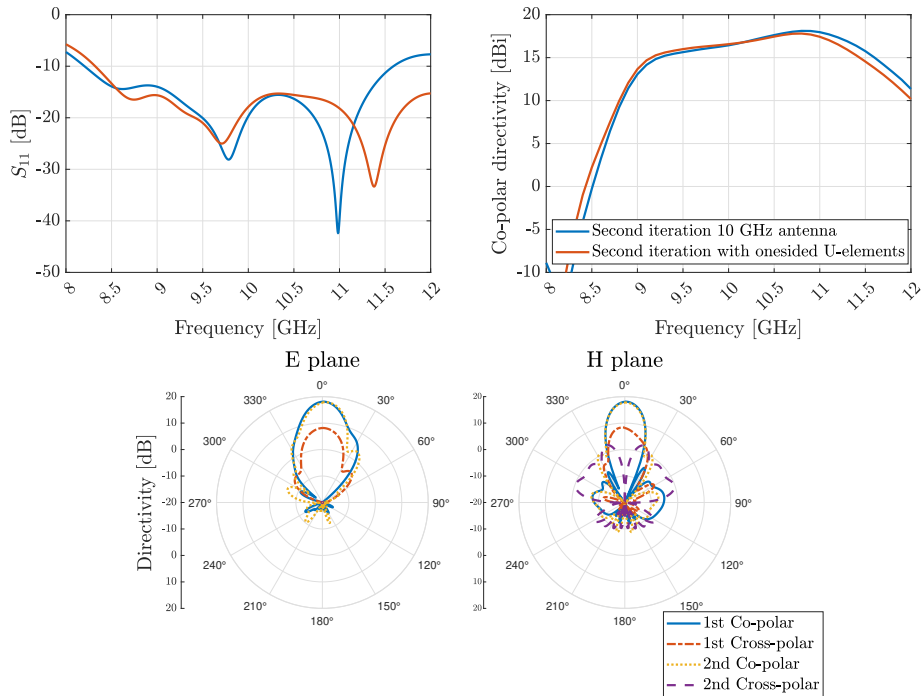


Figure 5.23: Performance of 10 GHz antennas with the V-shaped reflector

Chapter 6

Antenna realisation and measurements

6.1 Realisation of antennas

PCB design

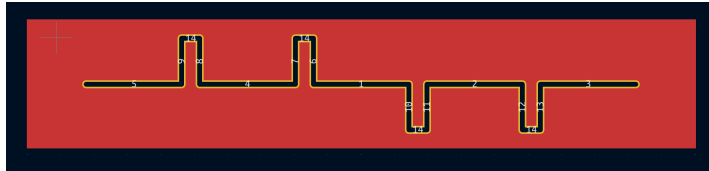


Figure 6.1: 10 GHz Franklin slot antenna PCB designed in KiCad software

In total, four Franklin slot antennas were designed for production. These are the 10 GHz first iteration antenna, the 10 GHz second iteration antenna, the 10 GHz second iteration antenna with all phasing elements on one side and the 2.5 GHz antenna. Their respective dimensions and simulation results are in section 5.3. We designed PCBs for these antennas in KiCad 7.0 [13].

We drew three overlapping rectangular layers for the top copper, top mask removal, and the edge cuts board outline of length l_{gnd} and width w_{gnd} . We then drew the slot with multiple overlapping oval through-hole pads. Finally, we exported the Gerber files required for PCB production.

Realised antennas

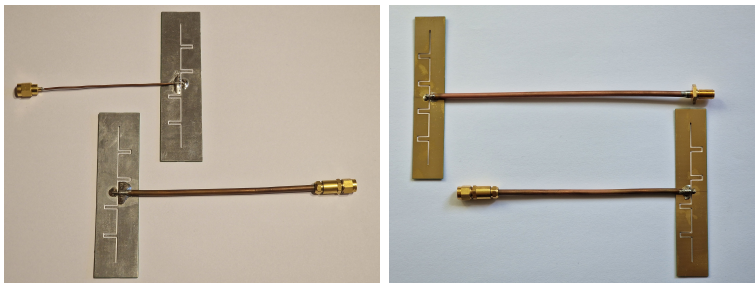


Figure 6.2: All four realised versions of 10 GHz Franklin slot antennas

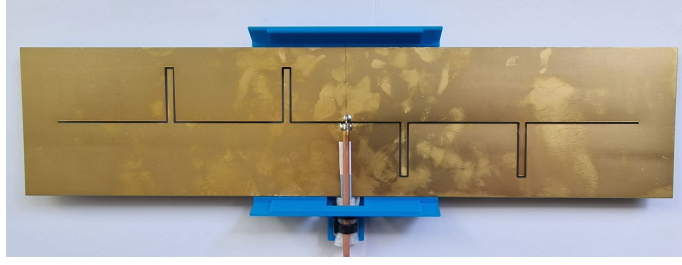


Figure 6.3: 2.5 GHz Franklin slot antenna with its holder

We had JLCPCB [14] manufacture these PCBs for us. The first iteration of the 10 GHz antenna was made with a 0.8 mm FR4 substrate and hot air solder levelling (HASL) finish because of its cost. The other antennas were made with a thinner substrate of 0.6 mm. This decreased thickness has led to problems during the HASL procedure, especially for the large 2.5 GHz antenna. We had to proceed with an electroplated nickel immersion gold (ENIG) surface finish instead, which gave these antennas a golden colour. The ENIG can be problematic for higher-frequency applications due to the ferromagnetic properties of nickel [15], but it is negligible for our antennas.

We then soldered 50Ω semi-rigid coaxial cables to these antennas. Two different coaxial cables were attached to the first iteration of the antenna, one being thicker with $r_a = 0.4$ mm and the other much thinner. The other antennas were realised only with the thicker coaxial cable.

The slot of realised antennas is slightly different due to the manufacturing process, as the outer edges are rounded. This difference, however, has no significant impact on the antenna performance, as verified by simulation.

■ Realised reflectors

We created two reflectors, one being flat and the other being V-shaped. The flat reflector was only used with the first iteration of 10 GHz antennas, while the V-shaped one was used with the second iteration of 10 GHz antennae. We created these reflectors out of 1.6 mm FR4 copper-clad with the dimensions from section 5.4. We then 3D-printed holders for these reflectors out of PLA plastic. These holders have an L-bracket on the back for mounting that we can adjust for the antenna's vertical and horizontal orientations and two arms to hold the 10 GHz antennas with adjustable spacing d_{ref} . The V-shaped reflector holder is also used to hold the 2.5 GHz antenna.

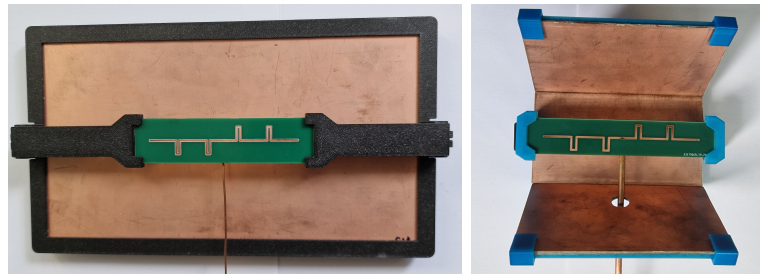


Figure 6.4: Flat reflector and the V-shaped reflector for 10 GHz antennas

6.2 Measurement setup

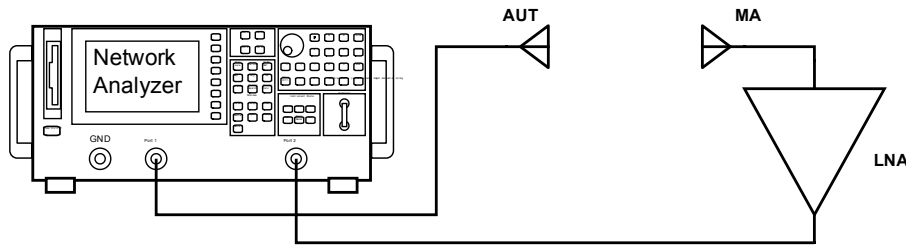


Figure 6.5: Setup used for measuring radiation patterns and directivity

We measured these antennas in the RF anechoic chamber of the Department of Electromagnetic Field with a Rohde&Schwarz ZVA40 vector network analyser (VNA). An anechoic chamber is necessary for antenna measurements to eliminate reflections from the surroundings and ensure that only the direct beam between two antennas is measured. In Figure 6.6, we see this anechoic chamber with a fixed measuring antenna (MA) at the far end and our antenna under test (AUT) placed on a rotating pedestal. Figure 6.5 shows that the antenna under test is directly connected to port 1 of a vector network analyser. In contrast, the measuring antenna is connected to a low-noise amplifier (LNA) with a gain of 20 dB, which output is then connected to port 2 of the VNA. We utilised the LNA to raise the received signal level at the measurement antenna to decrease the VNA sweep time for faster measurements without losing the received signal in the VNA noise floor.

We first measured the matching of our antennas by measuring S_{11} with the VNA with a calibrated port 1. We then measured gain for our antennas by measuring S_{21} transmission parameter between the two VNA ports for all directions with the step of one degree. In this case, our antenna under test is the transmitting antenna, and the measuring antenna is the receiving. We did this for both E and H antenna planes and antenna polarisations. We then measured an antenna with known gain as an antenna under test to obtain a reference to calculate absolute gain values for our measured antennas.

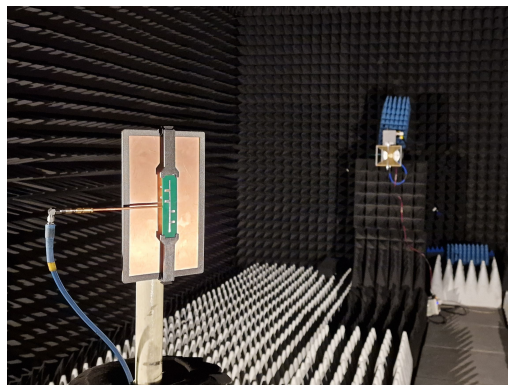


Figure 6.6: Antenna with a flat reflector in the RF anechoic chamber

6.3 Measurements of realised antennas

Measured antenna matching

In the following figures, we can see the measured S parameters together with their simulations from section 5.3. We can see that the 2.5 GHz antenna S_{11} matches well with the simulated model with only a slightly smaller matching bandwidth of 29.3 %. The simulated models do not align as well with the 10 GHz antennas. We can see that these measured results are more rippled than the simulated models. This ripple is especially significant on the antenna with

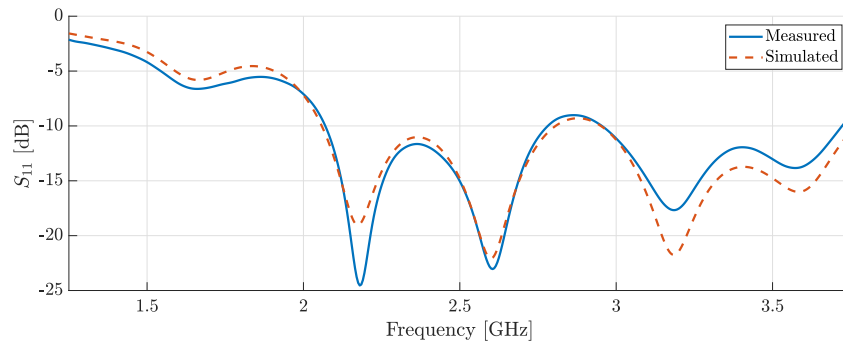


Figure 6.7: S_{11} for the 2.5 GHz antenna

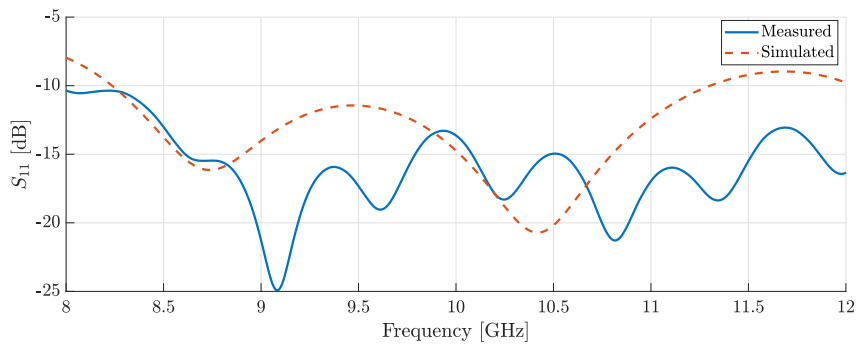


Figure 6.8: S_{11} for the 10 GHz second iteration antenna

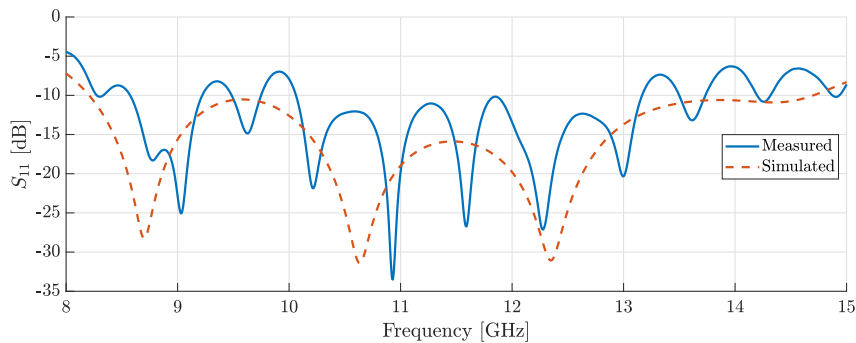


Figure 6.9: S_{11} for the 10 GHz antenna with one-sided phasing elements

one-sided phasing elements, as we used a different SMA coaxial connector rated only up to 8 GHz, which causes a lower bandwidth for our antenna. The other 10 GHz variation performs much better due to the use of a different SMA connector, and even though the ripple is still present, this measured antenna has a much greater matching bandwidth of 80.2 %, as shown in Figure 6.12. Figure 6.10 shows the difference between a first-iteration antenna with a flat reflector and a thick or thin coaxial cable, for which the thick cable performs better. Lastly, Figures 6.11 and 6.12 show the second iteration with the V-shaped reflector. This variant achieves a bandwidth of 76.6 % and offers a matching of -20 dB around frequency where its maximum gain is.

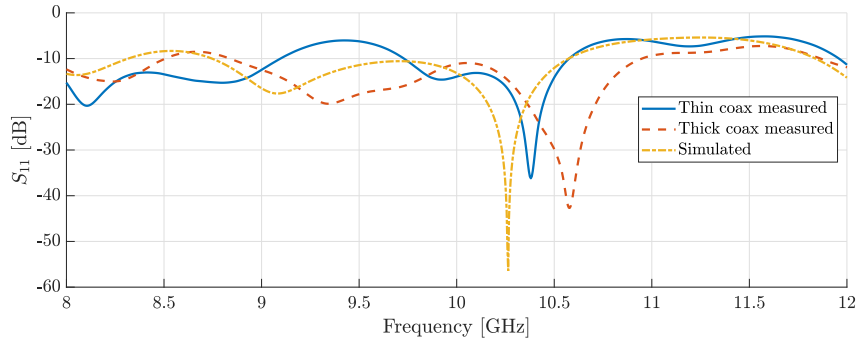


Figure 6.10: S_{11} for the 10 GHz first iteration antenna with the flat reflector

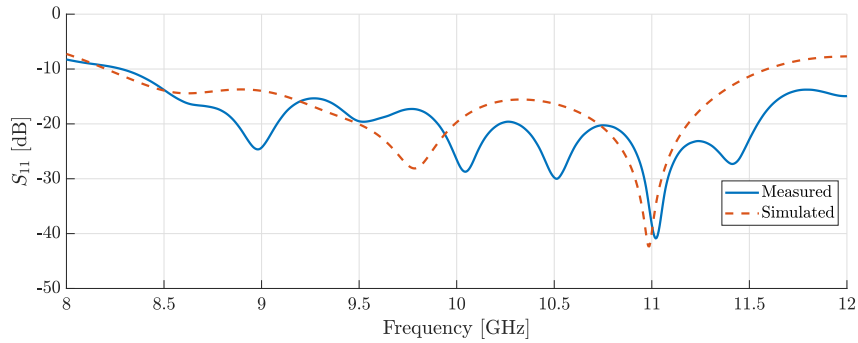


Figure 6.11: S_{11} for the 10 GHz second iteration antenna with the V reflector

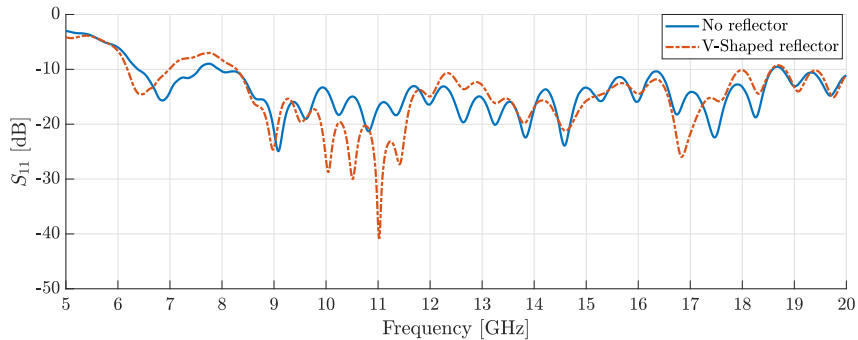


Figure 6.12: Broadband performance of the 10 GHz second iteration antenna

Measured antenna gain

The following figures show the measured antenna gain compared to the simulated directivity for these antennas from section 5.3. We plotted these values of gain and directivity for the direction of $\theta = 0^\circ$ and $\phi = 0^\circ$ for frequency. As we can see, the real antennas perform similarly to the simulated results. The 2.5 GHz antenna has a maximum gain of 9.7 dBi with a radiation bandwidth of 21.6 %. The second 10 GHz iteration antenna has a maximum gain of 11.1 dBi with a radiation bandwidth of 18.6 %, whilst the second iteration with the one-sided phasing elements has a maximum gain of 11.3 dBi with a radiation bandwidth of 14.2 %. Regarding the cross-polar directivity, the one-sided version performs the best, with it being less than -20 dBi.

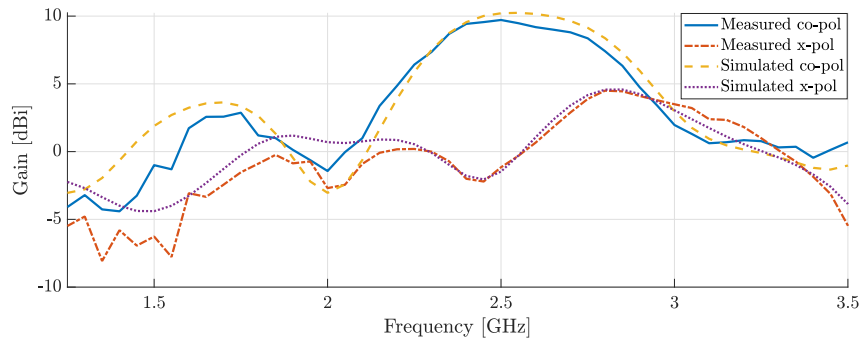


Figure 6.13: Gain for the 2.5 GHz antenna

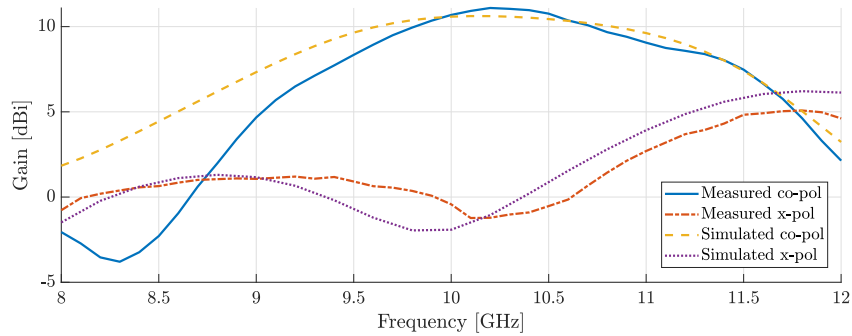


Figure 6.14: Gain for the 10 GHz second iteration antenna

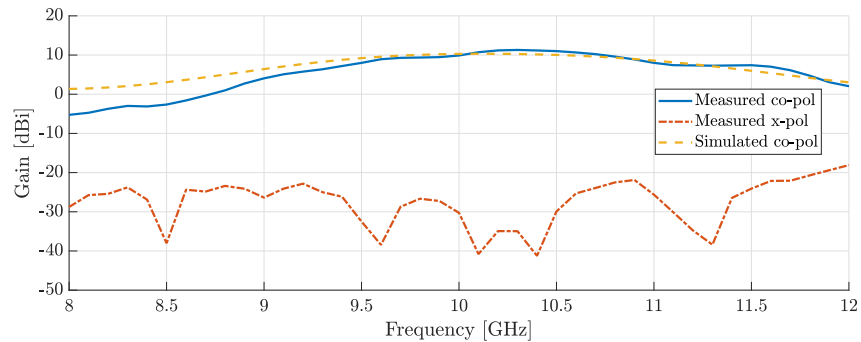


Figure 6.15: Gain for the 10 GHz antenna with one-sided phasing elements

Figures 6.16 and 6.17 show the gain for the variations with reflectors. The first iteration with the flat reflector has a maximum gain of 16.4 dBi with a radiation bandwidth of 9.8 %, whilst the second iteration with the V-shaped reflector has a max gain of 18.1 dBi with a radiation bandwidth of 18.4 %.

Figure 6.18 shows the radiation patterns for three antennas at the frequency for their maximum gains. We can see that the measured radiation patterns

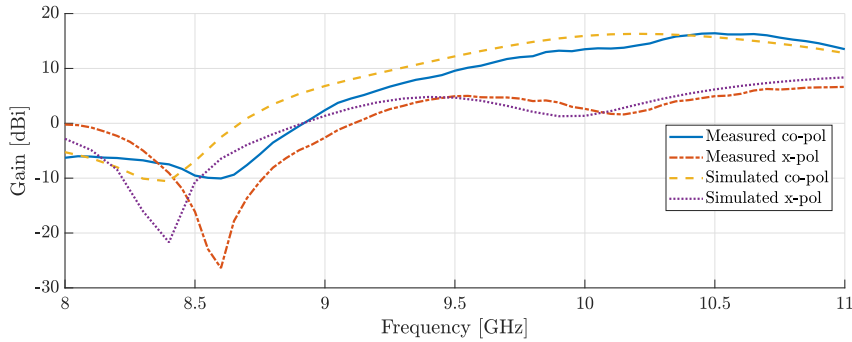


Figure 6.16: Gain for the 10 GHz first iteration antenna with the flat reflector

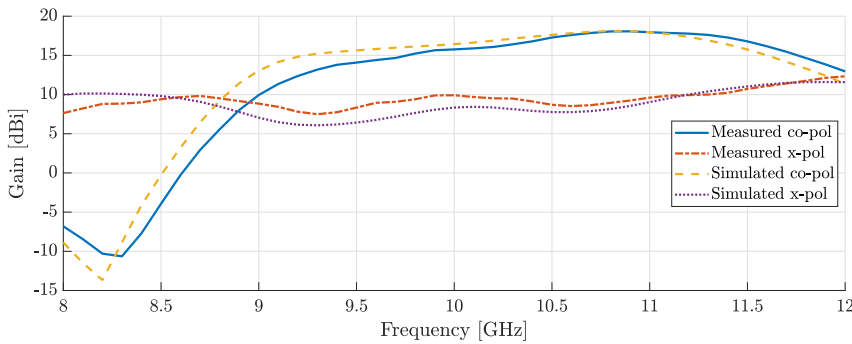


Figure 6.17: Gain for the 10 GHz second iteration antenna with the V reflector

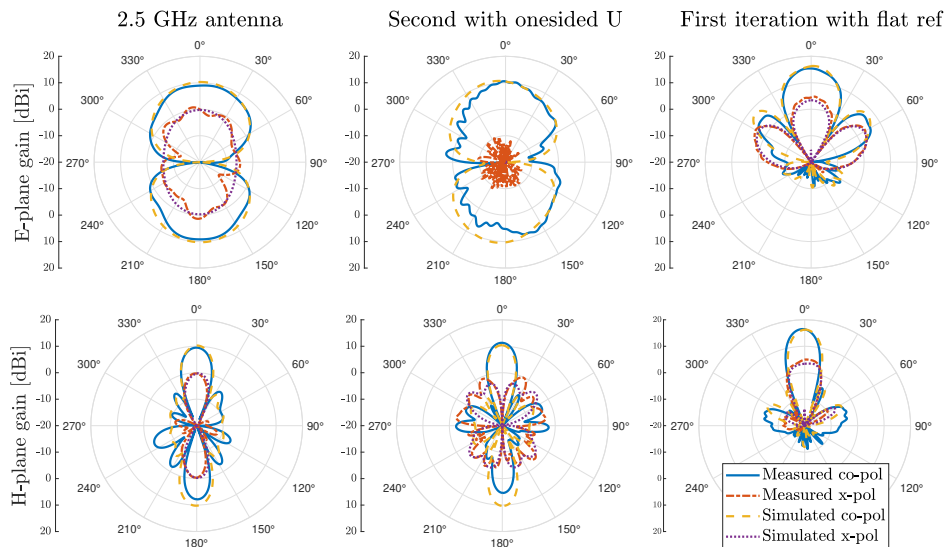


Figure 6.18: Radiation patterns for the following antennas

align with the simulated ones. The measurement stand and the holder affect the front-to-back ratio for the bidirectional antennas. There is also some ripple in the measured gain for the 10 GHz antennas without reflectors. We can also see a significant reduction in the cross-polar gain in the E-plane for the second iteration with one-sided phasing elements.

Figures 6.19 and 6.20 show the radiation patterns for the 10 GHz second iteration antenna without and with the V-shaped reflector for the maximum gain frequency and the lower and upper BW_r limit frequencies. We can see that these measured radiation patterns once again align with the measured ones and that the cross-polar gain increases with frequency.

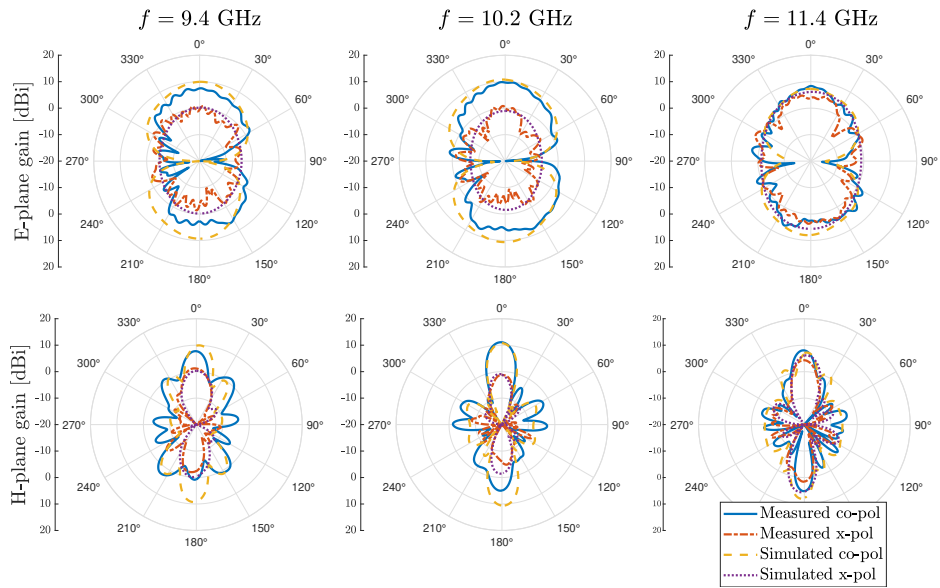


Figure 6.19: Radiation patterns for the 10 GHz second iteration antenna

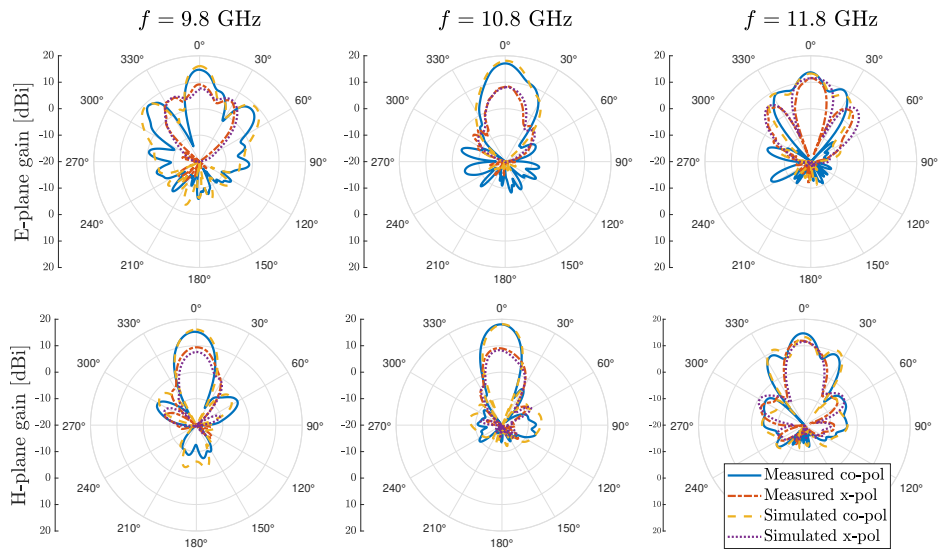


Figure 6.20: Radiation patterns for 10 GHz antenna with the V-shaped reflector



Conclusion

This thesis examines slot antennas with a cutout in the shape of a Franklin antenna and a coaxial cable feed. It was shown that these Franklin slot antennas can be viable antenna structures. These antennas can be easily matched to a commonly used 50Ω impedance without any impedance transformers necessary and achieve a very broad matching bandwidth. These antennas also boast increased directivity compared to the simple slot antenna or the Franklin antenna and have a bidirectional radiation pattern.

We used the CST studio suite to conduct full-wave analysis in the time domain solver for thin PEC-sheet Franklin slot antennas. We have shown that the five-element Franklin slot antenna performs the best, as the three-element variant struggles with matching bandwidth. In contrast, antennas with more than five radiating elements struggle with radiation bandwidth and only provide a negligible increase in directivity. We examined multiple variants of the five-element Franklin slot with differently oriented phasing elements and chose two viable structures. One of these has phasing elements on half of the antenna facing the same direction but facing the opposite direction on the other half, whilst the other one has all the phasing elements facing the same direction. The first variant has a broader radiation bandwidth, whilst the second one has lower cross-polarisation levels in the main radiating direction.

We then modelled the Franklin slot antennas as a copper layer on an FR4 substrate again in CST. We have shown that if the Franklin cutout also involves the FR4 substrate and the inner cutout walls are metallised, then the negative influence of the FR4, which causes an operating frequency shift and dielectric losses, is mostly eliminated.

When designing a Franklin slot antenna, the ground plane width w_{gnd} , the slot width w_{slot} and substrate thickness h_{FR4} should be chosen with significant consideration for the best antenna performance. The inner conductor radius r_{a} of coaxial cable used should not be too thin as it would lead to lousy impedance matching, ideally at least one-third of the slot width. The coaxial cable can be directly soldered onto the antenna without any balun, unlike the dipole of Franklin antennas, where using baluns is necessary to eliminate the common mode currents. We can realise such a Franklin slot antenna as a PCB antenna with standard PCB-making processes, as the metallised slots are commonly used for mounting through-hole components.



Bibliography

- [1] N. Mohamed Mohamed-Hicho, E. Antonino-Daviu, M. Cabedo-Fabrés, and M. Ferrando-Bataller, “Designing slot antennas in finite platforms using characteristic modes,” *IEEE Access*, vol. 6, pp. 41346–41355, 2018.
- [2] C. Franklin, “Improvements in wireless telegraph and telephone aerials,” *UK British Patent GB242342*, 1925.
- [3] S.-Y. Chen and P. Hsu, “Open-ended rampart slot array antenna fed by a cpw,” *IEEE Antennas and Wireless Propagation Letters*, vol. 4, pp. 320–322, 2005.
- [4] S.-Y. Chen, I.-C. Lan, and P. Hsu, “In-line series-feed collinear slot array fed by a coplanar waveguide,” *IEEE Transactions on Antennas and Propagation*, vol. 55, no. 6, pp. 1739–1744, 2007.
- [5] Y. Cheng and Y. Dong, “Circularly polarized rampart slotline terminated with patch for low-cost applications,” in *2021 IEEE International Symposium on Antennas and Propagation and USNC-URSI Radio Science Meeting (APS/URSI)*, pp. 787–788, 2021.
- [6] Dassault Systèmes, “Cst studio suite | simulia - dassault systèmes.” <https://www.3ds.com/products/simulia/cst-studio-suite>. Accessed: 2024-5-12.
- [7] C. A. Balanis, *Antenna theory: analysis and design*. John Wiley & sons, 2016.
- [8] S. Orfanidis, *Electromagnetic Waves and Antennas*. Sophocles J. Orfanidis, 2016. Available: <https://www.ece.rutgers.edu/~orfanidi/ewa/> (visited: 2024-4-23).
- [9] Y. Huang, *Antennas: from theory to practice*. John Wiley & Sons, 2021.
- [10] S. Gibilisco, “Gain of a collinear antenna array.” <https://www.youtube.com/watch?v=DFRe7ttChwc>, 2009. Accessed: 2023-11-18.
- [11] W. L. Stutzman and G. A. Thiele, *Antenna theory and design*. John Wiley & Sons, 2012.

